Crust and uppermost mantle beneath the North China Craton, northeastern China, and the Sea of Japan from ambient noise tomography

Yong Zheng,[1] Weisen Shen,[2] Longquan Zhou,[3] Yingjie Yang,[1,4] Zujun Xie,[1] and Michael H. Ritzwoller[2]

Received 28 June 2011; revised 30 October 2011; accepted 2 November 2011; published 21 December 2011.

[1] A 3-D shear velocity model of the crust and uppermost mantle to a depth of 100 km is presented beneath the North China Craton (NCC), northeastern China, the Korean Peninsula, and the Sea of Japan. Ambient noise Rayleigh wave tomography is applied to data from more than 300 broadband seismic stations from Chinese provincial networks (CEArray), the Japanese F-Net, and the IRIS Global Seismic Network. Continuous data from 2007 to 2009 are used to produce group and phase velocity maps from 8 s to 45 s periods. The model is motivated to constrain the distributed intraplate volcanism, crustal extension, cratonic rejuvenation, and lithospheric thinning that are hypothesized for the study region. Numerous robust features are observed that impose new constraints on the geometry of these processes, but discussion concentrates only on four. (1) The North-South Gravity Lineament follows the ~40 km contour in crustal thickness, and crustal thickness is anticorrelated with water depth beneath the Sea of Japan, consistent with crustal isostasy for a crust with laterally variable composition. (2) The lithosphere is thin (~70 km) beneath the Songliao-Bohai Graben but seismically fast. (3) Even thinner more attenuated lithosphere bounds three sides of the eastern NCC (in a horseshoe shape), identifying a region of particularly intense tectonothermal modification where lithospheric rejuvenation may have reached nearly to the base of the crust. (4) Low-velocity anomalies reach upward (in a Y shape) in the mantle beneath the eastern and western borders of the Sea of Japan, extending well into continental East Asia in the west, and are separated by a ~60 km thick lithosphere beneath the central Sea of Japan. This anomaly may reflect relatively shallow slab dehydration in the east and in the west may reflect deeper dehydration and convective circulation in the mantle wedge overlying the stagnant slab.

Citation: Zheng, Y., W. Shen, L. Zhou, Y. Yang, Z. Xie, and M. H. Ritzwoller (2011), Crust and uppermost mantle beneath the North China Craton, northeastern China, and the Sea of Japan from ambient noise tomography, *J. Geophys. Res.*, *116*, B12312, doi:10.1029/2011JB008637.

1. Introduction

[2] The goal of this study and companion papers by *Yang et al.* [2010], Y. Yang et al. (A synoptic view of the distribution and connectivity of the mid-crustal low velocity zone beneath Tibet, submitted to *Journal of Geophysical Research*, 2011), *Zheng et al.* [2010b], and L. Zhou et al. (Ambient noise surface wave tomography of South China, submitted to *Geophysical Journal International*, 2011) is to advance toward an integrated, highly resolved shear velocity (Vs) model of the crust and uppermost mantle beneath China. Zhou et al. (submitted manuscript, 2011) focus on Southeast China, and *Yang et al.* [2010], Yang et al. (submitted manuscript, 2011), and *Zheng et al.* [2010b] focus on western China and Tibet. The complementary focus of the current paper is the Sino-Korean Craton, northeastern China, the Korean Peninsula, and the Sea of Japan. More than 320 seismic stations from Chinese provincial networks in northeastern China and surrounding areas, Japanese F-Net stations [*Okada et al.*, 2004], and IRIS GSN stations are the basis for this study (Figure 1). The resulting station and path coverage that emerges is unprecedented in this region. In order to place strong constraints on crustal structure, ambient noise tomography is employed. As described below, ambient noise tomography has already been applied in other regions of China (e.g., Tibet), at larger scales (e.g., across all of China) at a lower resolution, or in a part of the study region (e.g., North China Platform, Korean peninsula), but a resulting integrated, high-resolution model of the crust and uppermost mantle of the entire region of study has never before been

[1]State Key Laboratory of Geodesy and Earth's Dynamics, Institute of Geodesy and Geophysics, Chinese Academy of Sciences, Wuhan, China.
[2]Center for Imaging the Earth's Interior, Department of Physics, University of Colorado at Boulder, Boulder, Colorado, USA.
[3]China Earthquake Network Center, Beijing, China.
[4]Australian Research Council Centre of Excellence for Core to Crust Fluid Systems/GEMOC, Department of Earth and Planetary Sciences, Macquarie University, North Ryde, New South Wales, Australia.

0148-0227/11/2011JB008637

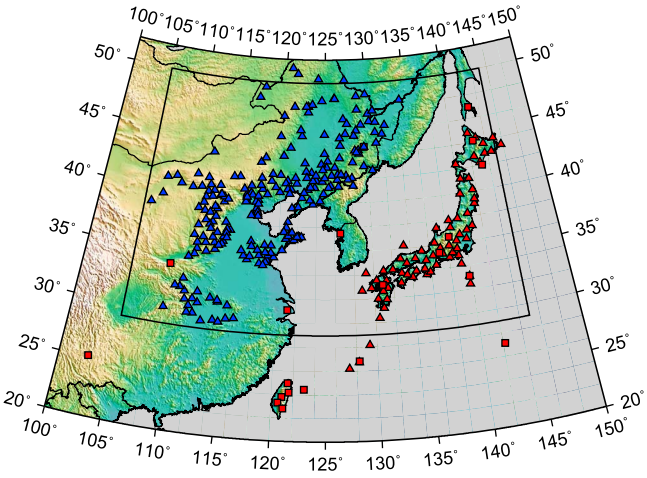

Figure 1. The broadband seismic stations used in this study. The blue triangles are the Chinese provincial broadband seismic stations (CEArray), the red triangles are the F-Net long-period stations, and the red squares are other broadband stations, mostly from the IRIS GSN. The black box defines the study region.

constructed. Such a model is desired to illuminate a set of interconnected tectonic problems that make the Sino-Korean Craton, northeastern China, and the Sea of Japan a particularly fertile area for seismic tomography.

[3] Northeastern China is composed of a mosaic of tectonic blocks and lineated orogenic belts (Figure 2) that have been arranged and modified by a long, complex, and in some cases enigmatic history of subduction, accretion, and collision dating back to the Archean [e.g., *Sengor and Natal'in*, 1996; *Yin and Nie*, 1996; *Yin*, 2010]. In the south, the Sino-Korean Craton (SKC), delineated by solid red lines in Figure 2, is separated from the Yangtze Craton to the south by the Qinling-Dabie-Sulu orogenic belt [*Yin and Nie*, 1993]. The SKC itself consists of the Ordos Block, the North China Platform, Bohai Bay, the Korean Peninsula, as well as marginal and intruding mountain ranges. The Chinese part of the SKC is usually referred to as the North China Craton (NCC) and is divided here into western, central, and eastern parts delineated by dashed red lines. North of the SKC, the Xing'an–East Mongolia block is separated from the Songliao-Bohai graben by the North-South Gravity Lineament (NSGL). The NSGL extends southward into the SKC near the boundary between the central and eastern parts of the North China Craton. The Songliao-Bohai graben, stretching from the Songliao Basin to the Bohai Gulf, is flanked to the east by the Tancheng-Lujiang (Tanlu) Fault that extends into the SKC and forms the eastern boundary of the North China Craton. The Tanlu Fault also defines the western border of the Northeast Asia Fold Belt [e.g., *Sengor and Natal'in*, 1996; *Yin and Nie*, 1996].

[4] Much of northeastern China has undergone extensive tectonism during the late Mesozoic and Cenozoic eras [e.g., *Yin*, 2010]. Northeastern China, bounded by the SKC to the south and the Sea of Japan back-arc basin to the east, is part of eastern China's Cenozoic volcanic zone [e.g., *Ren et al.*, 2002]. Episodic volcanism has been particularly prominent along three volcanic mountain chains: Great Xing'an Range (GXAR), Lesser Xing'an Range (LXAR), Changbai Mountains (CBM). Rifting and extension are believed to have begun in the late Mesozoic [*Tian et al.*, 1992] and have led to the development of the Songliao Basin, although the Songliao basement is traced back to the Archean [*Rogers and Santosh*, 2006]. It has also been hypothesized that there is a physical linkage between the sequential openings of the Songliao graben [e.g., *Liu et al.*, 2001] and the Sea of Japan [*Tatsumi et al.*, 1989; *Jolivet et al.*, 1994]. The SKC formed largely in the Archean, but it is a paradigm of an Archean craton that has lost its lithospheric keel. Petrological and geochemical evidence [e.g., *Menzies et al.*, 1993; *Griffin et al.*, 1998] suggests that typical cratonic lithosphere existed beneath the entire SKC until at least the Ordovician, after which the SKC was reactivated and lithospheric thinning occurred at the minimum beneath the eastern part of the NCC.

[5] The physical mechanisms that have produced the highly distributed volcanism, crustal extension, cratonic rejuvenation and lithospheric thinning that have occurred across parts of northeastern China remain poorly understood [e.g., *Deng et al.*, 2007; *Chen*, 2010]. These issues can be illuminated with seismic images of velocity heterogeneities, internal discontinuities, and crustal and mantle anisotropy, yet the vast majority of the studies to date have been geochemical or petrological in nature. Increasingly,

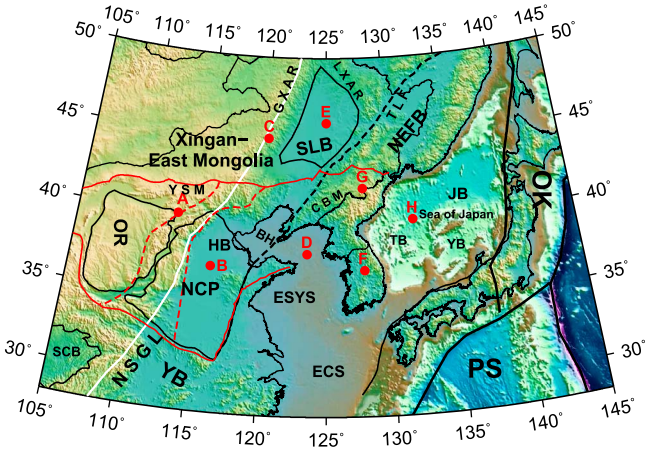

Figure 2. The geological setting of this study. Solid red lines mark the boundaries of the Sino-Korean Craton (SKC), the solid white line identifies the North-South Gravity Lineament (NSGL), the dashed black line is the Tancheng-Lujiang fault (TLF), and solid black lines outline blocks and tectonic boundaries [*Zhang et al.*, 2003]. The North China Craton is the part of the SKC in China and is subdivided by dashed red lines into western, central, and eastern parts. Feature names are abbreviated as follows: PS, Philippine Sea Plate; OK, Okhotsk Plate; NCP, North China Platform; YB, Yangtze Block; SLB, Songliao Basin; JB, Japan Basin; YB, Yamato Basin; TB, Tsushima Basin; SB, Sichuan Basin; OR, Ordos Block; BH, Bohai Bay; GXAR, Great Xing'an Range; LXAR, Lesser Xing'an Range; CBM, Changbai Mountain Range; YSM, Yinshan Mountain Range; ESYS, East Shandong Yellow Sea Block; NEFB, Northeast Asian Fold Belt; NSGL, North-South Gravity Lineament; and HB, Huabei Basin. Red dots with letters mark locations of the dispersion curves and 1-D shear velocity profiles shown in Figures 11 and 12.

seismological studies are adding new information due in part to the rapid expansion of seismic instrumentation in China over the past few years [e.g., *Zheng et al.*, 2010a]. These studies include body wave tomography of the mantle [e.g., *Lebedev and Nolet*, 2003; *Huang and Zhao*, 2006; *Zhao*, 2009; *Tian et al.*, 2009; *Xu and Zhao*, 2009; *Li and van der Hilst*, 2010; *Santosh et al.*, 2010] and of the crust [e.g., *Sun and Toksöz*, 2006]. Pn tomography [*Li et al.*, 2011], receiver functions analyses [*Zheng et al.*, 2006; *Chen et al.*, 2009], and shear wave splitting studies have also been performed [*Zhao et al.*, 2008; *Bai et al.*, 2010; *Li and Niu*, 2010]. Recent body wave results have focused mainly on the eastern part of the NCC, including efforts to image its thin intact lithosphere as well as the potential remnants of the delaminated lithosphere near 400 km depth [e.g., *Chen et al.*, 2009; *Xu and Zhao*, 2009].

[6] At least parts of northeast China have been imaged by larger-scale teleseismic surface wave dispersion studies [e.g., *Ritzwoller and Levshin*, 1998; *Ritzwoller et al.*, 1998; *Villaseñor et al.*, 2001; *Yanovskaya and Kozhevnikov*, 2003; *Huang et al.*, 2003, 2004; *Priestley et al.*, 2006]. Recent regional-scale teleseismic surface wave studies have also been conducted within North China [e.g., *Tang and Chen*, 2008; *Huang et al.*, 2009; *Zhou et al.*, 2009; *He et al.*, 2009; *Pan et al.*, 2011], in adjacent regions [e.g., *Yao et al.*, 2006, 2008], and in the Sea of Japan [e.g., *Bourova et al.*, 2010; *Yoshizawa et al.*, 2010]. Some of these studies are discussed further in the context of our 3-D model in section 6.

[7] Within the last few years a new method of surface wave tomography has emerged based on using ambient seismic noise to extract surface wave empirical Green's functions (EGFs) and to infer Rayleigh [e.g., *Sabra et al.*, 2005; *Shapiro et al.*, 2005] and Love wave [e.g., *Lin et al.*, 2008] group and phase speeds in continental areas. Compared with traditional earthquake tomography methods, ambient noise tomography is relatively free of artifacts related to the distribution of earthquakes as well as errors in earthquake locations and source mechanisms. The dominant frequency band for ambient noise tomography lies between about 8 and 40 s period. Rayleigh waves in this band are sensitive to crustal and uppermost mantle structures. Ambient noise tomography has produced phase and group velocity maps in various regions around the world [e.g., *Moschetti et al.*, 2007; *Yang et al.*, 2007; *Villaseñor et al.*, 2007; *Bensen et al.*, 2008] and also is the basis for 3-D crustal and uppermost mantle models of isotropic shear velocity structure [e.g., *Yang et al.*, 2008a, 2008b; *Bensen et al.*, 2009; *Moschetti et al.*, 2010b], radial anisotropy [e.g., *Moschetti et al.*, 2010a], and azimuthal anisotropy [e.g., *Lin et al.*, 2011]. Ambient noise in east Asia has been shown to be sufficiently well distributed in azimuthal content to be used for surface wave dispersion measurements [e.g., *Yang and Ritzwoller*, 2008] and studies based on ambient noise have been conducted at large scales across all of China [*Zheng et al.*, 2008; *Sun et al.*, 2010], in regions adjacent to northeastern China [e.g., *Yao et al.*, 2006, 2008; *Guo et al.*, 2009; *Li et al.*, 2009; *Huang et al.*, 2010; *Yang et al.*, 2010; *Zheng et al.*, 2010b; Zhou et al., submitted manuscript, 2011], within the North China Craton [*Fang et al.*, 2010], on the Korean Peninsula [*Kang and Shin*, 2006; *Cho et al.*, 2007], and in Japan [e.g., *Nishida et al.*, 2008].

[8] Ambient noise tomography in northeastern China, the Korean Peninsula, the Sea of Japan, however, is faced with an uncommon technical challenge – the existence of a persistent localized microseismic source on Kyushu Island [*Zeng and Ni*, 2010] in the period band between about 8 and 14 s, which has been explained to be caused by long-period volcanic tremors beneath Aso Volcano in the center of Kyushu [*Kawakatsu et al.*, 2011; *Zeng and Ni*, 2011]. This signal causes a significant disturbance that is observable on cross correlations of ambient noise, which, if left uncorrected, would bias measurements of group and phase velocity in this period band of considerable sensitivity to crustal structure. A principal focus of this paper, therefore, is to identify this disturbance and minimize its effects on the estimated Rayleigh wave group and phase velocity dispersion maps.

[9] The present paper is based on Rayleigh wave group and phase velocity maps from 8 to 45 s period across the Sino-Korea Craton, northeastern China, Korea, and the Sea of Japan. Based on these maps, a 3-D model of the crust and uppermost mantle is constructed by Monte Carlo inversion along with associated uncertainties. The resulting information complements existing and emerging teleseismic body wave and surface studies by presenting new and much stronger constraints on the structure of the crust and uppermost mantle. The data processing and quality control procedures are described in section 2 and methods used to desensitize the data to degradation caused by the persistent, localized Kyushu microseism are presented in section 3. The Rayleigh wave group and phase velocity maps are described in section 4. Section 5 presents a brief discussion of the Monte Carlo inversion method. Section 6 describes the features of the resulting model. In addition, there is a discussion of several key findings including the relation between seafloor depth and crustal thickness beneath the Sea of Japan, the horseshoe shape (in map view) of the thinnest lithosphere that bounds the NCC, and the Y-shaped asthenosphere (on vertical profiles) observed beneath the Sea of Japan and the Northeast Asian Fold Belt.

2. Data Processing and Quality Control

[10] The data used in this study are continuous seismic waveforms recorded at broadband stations that existed in and around northeast China and the Sea of Japan from August 2007 to July 2009. Networks providing data include (1) Chinese Provincial Networks in northeast China consisting of 232 broadband seismic stations (referred to here as CEArray), (2) F-Net in Japan comprising 69 long-period seismic stations, and (3) the IRIS GSN broadband network in northeast Asia consisting of 22 stations. In total, 2 years of continuous waveform data have been acquired that were recorded at the 323 stations denoted by solid triangles and squares in Figure 1. Only vertical component data are processed, meaning only Rayleigh waves are studied.

[11] The data processing procedures follow those of *Bensen et al.* [2007] and *Lin et al.* [2008]. After removing the instrument responses, all records are band-pass filtered between 5 and 150 s period. We apply both temporal normalization and spectral whitening. Temporal normalization is applied in an 80 s moving window. Cross correlations are performed daily between all pairs of stations and then are

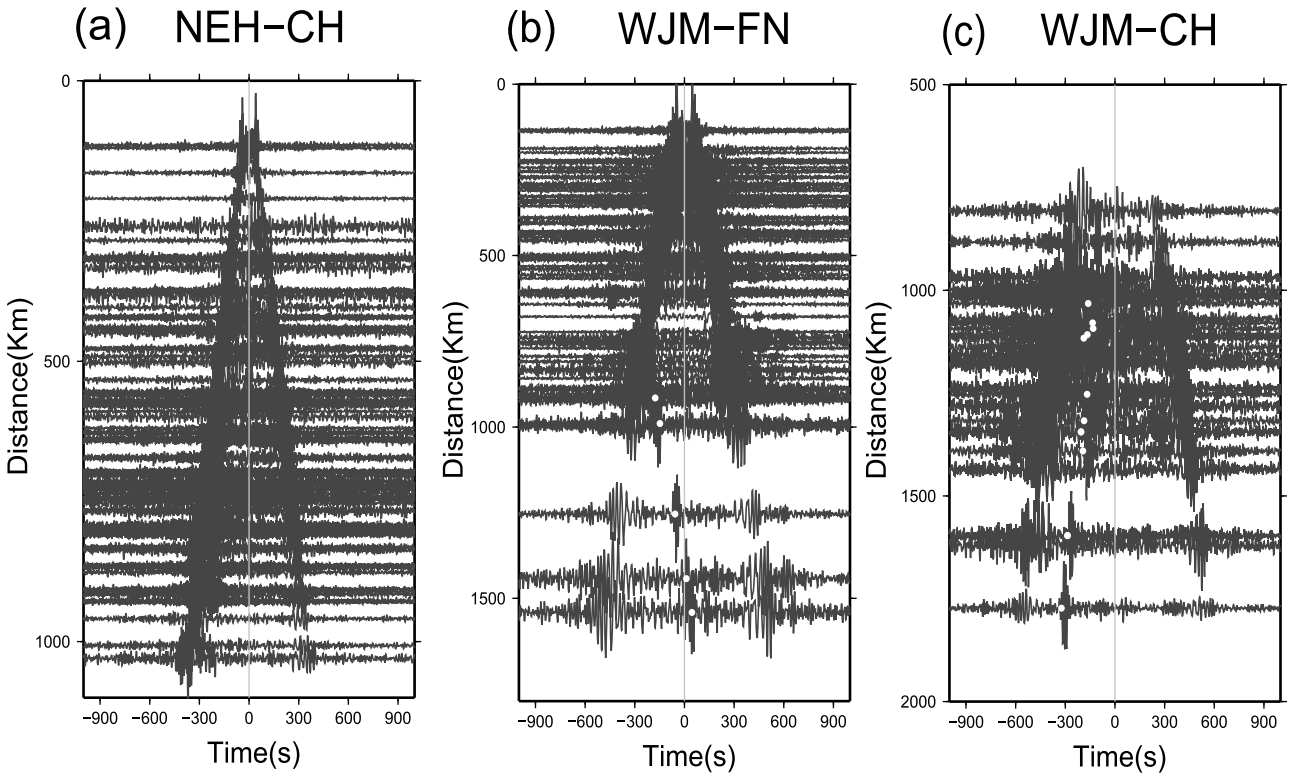

Figure 3. Record sections of cross correlations obtained from 2 years of waveform data (a) between Chinese provincial network stations, (b) between F-Net stations, and (c) between the Chinese stations and F-Net stations. The white dots identify the expected arrival times for the Kyushu persistent microseism.

stacked over the 2 year time window. Figure 3 presents example cross-correlation record sections among Chinese stations, among F-Net stations, and interstation pairs between F-Net stations and Chinese stations.

[12] Data quality control is discussed here and in section 3 and consists of five principal steps, denoted A–E. Most of these steps are based on procedures summarized by *Bensen et al.* [2007] and *Lin et al.* [2008], but because of the mixture of instrument types used in this study and the existence of the Kyushu microseism we add extra steps to ensure the reliability of the resulting dispersion measurements. In step A, a dispersion measurement is retained for a cross correlation at a given period only if signal-to-noise ratio (SNR) > 15 at that period, where SNR is defined by *Bensen et al.* [2007]. In step B, we remove the effects of the Kyushu microseism, which we discuss further in section 3. In step C, we retain an observation at a given period only if both the group and phase velocities are measured by the automated frequency-time analysis method [*Bensen et al.*, 2007]. Group and phase velocity are separate measurements and are not constrained to agree even though they are related theoretically [e.g., *Levshin et al.*, 1999]. In step D, we identify and discard stations with bad instrument responses. Step E is broken into two parts. First, we only accept dispersion measurements with path lengths ≥3 wavelengths. Second, a measurement is retained only if the misfit determined from the final dispersion map is less than 12 s for group travel time and less than 5 s for phase travel time, which is somewhat more than twice the standard deviation of the final misfit. Group and phase velocity dispersion measurements of Rayleigh waves are obtained on the symmetric component of interstation cross correlations except for paths identified as affected by the Kyushu microseism, as discussed further in section 3.

[13] Because the seismic instruments used in this study differ in origin between China, Japan, and the U.S., and instruments can vary within CEArray between provinces in China, it is important to identify errors and inconsistencies in response files. For the IRIS network data, F-Net data and most of the Chinese stations, full response (RESP) files including both analog and digital filter stages are available. For a small number of Chinese stations we possess only pole-zero response files missing the digital filtering stages. We find that for the CEArray instruments, the analog pole-zero responses sometimes differ from the full responses computed from the RESP files for stations that have both types of response files. Therefore, we discard the Chinese stations for which we have not been able to acquire RESP files. This affected 36 stations, none of which are included in the 232 Chinese stations shown in Figure 1. Using these response files, all data are converted to velocity prior to cross correlation.

[14] Two other procedures are applied to find other instrument response errors. First, we identify polarity errors (π phase shift) that may represent a unit's error in the instrument by comparing P wave first motions observed across the array following deep, distant teleseisms. We also look for half-period misfits based on the final tomography maps at each period. These procedures identified seven stations with polarity errors that are discarded. Second, we compare the phase and group times measured on the positive

Table 1. Number of Measurements Retained After Each Step in Data Quality Control

Period (s)	Step A	Step B	Step C	Step D	Step E (Phase)	Step E (Group)
10	20,816	14,563	14,492	13,567	11,053	10,180
14	31,356	25,770	25,740	24,082	22,606	21,593
20	33,573	33,573	33,564	31,555	29,170	29,515
25	28,990	28,990	28,982	27,398	25,209	25,161
30	25,495	25,495	25,491	24,210	22,096	21,623
35	21,976	21,976	21,972	20,985	18,903	18,247
40	18,172	18,172	18,165	17,488	15,303	14,688
45	14,503	14,503	14,495	14,031	11,810	11,352

and negative lags of all cross correlations, which identifies timing errors as long as both lags have a high SNR [*Lin et al.*, 2007]. These procedures identified and discarded three Chinese stations.

[15] The 2π phase ambiguity inherent in phase velocity measurements is resolved iteratively, first based on phase velocities predicted by the 3-D model of *Shapiro and Ritzwoller* [2002] and then later on with increasingly refined phase velocity maps that are determined in this study.

[16] With more than 300 stations, in principal about 50,000 interstation cross correlations could be obtained. Quality control procedures reduce this number appreciably as Table 1 illustrates. After applying the selection criteria, we obtain between about 10,000 to 30,000 group and phase velocity measurements for tomography at periods ranging from 10 to 45 s, although the number of paths drops sharply below 10 s period.

3. The Effect of the Localized Persistent Kyushu Microseism

[17] In northeast China, a strong disturbance appears on the cross-correlation waveforms. The record sections shown in Figures 3b and 3c show this disturbance, which appears as precursory signals (identified by white dots) in addition to the expected surface wave part of the empirical Green's function. Another example is presented in Figure 4a, where the disturbance appears at positive correlation lag between 100 and 150 s, whereas the desired Rayleigh wave signal arrives much later and is seen clearly only on the negative correlation lag. The arrival of these disturbances near to the Rayleigh wave packets interferes with the ability to measure Rayleigh wave speeds accurately. In fact, the effect tends to bias Rayleigh waves fast, particularly for Rayleigh wave group velocities.

[18] These precursory signals are due to the persistent, localized Kyushu microseism that has been identified and located by *Zeng and Ni* [2010] on the island of Kyushu, Japan, within our study region. *Kawakatsu et al.* [2011] explain the signal as having originated from long-period volcanic tremor beneath Aso Volcano on Kyushu Island. The period band of this microseism is dominantly between 8 and 14 s, and it is somewhat reminiscent of the longer-period persistent 26 s microseism located in the Gulf of Guinea [e.g., *Shapiro et al.*, 2006]. We are interested in minimizing its interference with surface wave dispersion measurements across the study region. To do so, we have relocated it, confirming the location of *Zeng and Ni* [2010], and have developed a data processing procedure that allows reliable dispersion curves to be obtained across the Sino-Korean Craton, northeastern China, the Korean peninsula, and the Sea of Japan. The effect of the procedure, however, is to reduce the number of measurements in the region broadly surrounding Kyushu at periods between 10 and 18 s.

3.1. Relocation of the Kyushu Microseism

[19] We use the envelope functions between periods of 10 and 12 s for the Kyushu signal observed on interstation cross correlations to locate the Kyushu microseism. An example envelope function is shown in Figure 4a (bottom) Based on an initial observed group velocity map at 11 s period, we predict the theoretical arrival time of the Kyushu signal for each interstation pair for each hypothetical source location on a broad map of the region. We then take the observed amplitude of the envelope function at the predicted time and plot it at the hypothetical source location. An example is shown in Figure 4b, where the hyperbola identifies the set of possible locations for the Kyushu microseism for a particular interstation pair. We refer to this figure as the migrated envelope function. Finally, we stack over all migrated envelope functions for cross correlations involving the GSN stations INCN (Inchon, South Korea) and SSE (Shanghai, China), with the paths shown in Figure 4c. The resulting stack of migrated envelope functions is shown in Figure 4d, demonstrating that the relocation of the Kyushu microseism is close to the location from *Zeng and Ni* [2010] (Figure 4d) on Kyushu Island.

3.2. Eliminating the Effect of the Kyushu Microseism

[20] Assuming that the Kyushu microseism is a point source, for each interstation cross correlation we calculate the expected arrival time of the Kyushu signal as well as the theoretical arrival time of the Rayleigh wave between the two stations. The relative arrival times of the Kyushu signal (white dots in Figure 3) and the interstation Rayleigh waves are highly variable but systematic. When the arrival times of the Kyushu signals are close to the desired surface waves it becomes difficult to separate the signals between 8 and 14 s period on the symmetric component of the cross correlations. However, the systematics of the relative arrival times can be exploited to separate the two waves and obtain reliable Rayleigh wave group and phase velocity measurements for most paths by focusing on a single correlation lag. Figure 5 illustrates this point by showing how the Kyushu signal biases group and phase velocity measurements when the Rayleigh wave and the Kyushu signal arrive nearly simultaneously on the negative lag component of the cross correlation (Figure 5a). Figure 5b shows the symmetric component of the cross correlation. Figure 5c is the positive component of the cross correlation, which is free from the Kyushu disturbance. On frequency-time diagrams [e.g., *Ritzwoller and Levshin*, 1998], large differences between positive and negative correlation lag times are observed at periods shorter than 18 s, especially in the group velocity dispersion curves. This is illustrated by Figures 5d and 5e, in which the Kyushu signal disturbs the dispersion curve in Figure 5d but not Figure 5e. The Kyushu signal causes the measured group velocity to bias toward higher velocities (Figure 5f). At periods longer than 18 s, however, differences are quite small.

[21] Therefore, to separate the desired interstation Rayleigh wave from the Kyushu signal we must measure the Rayleigh

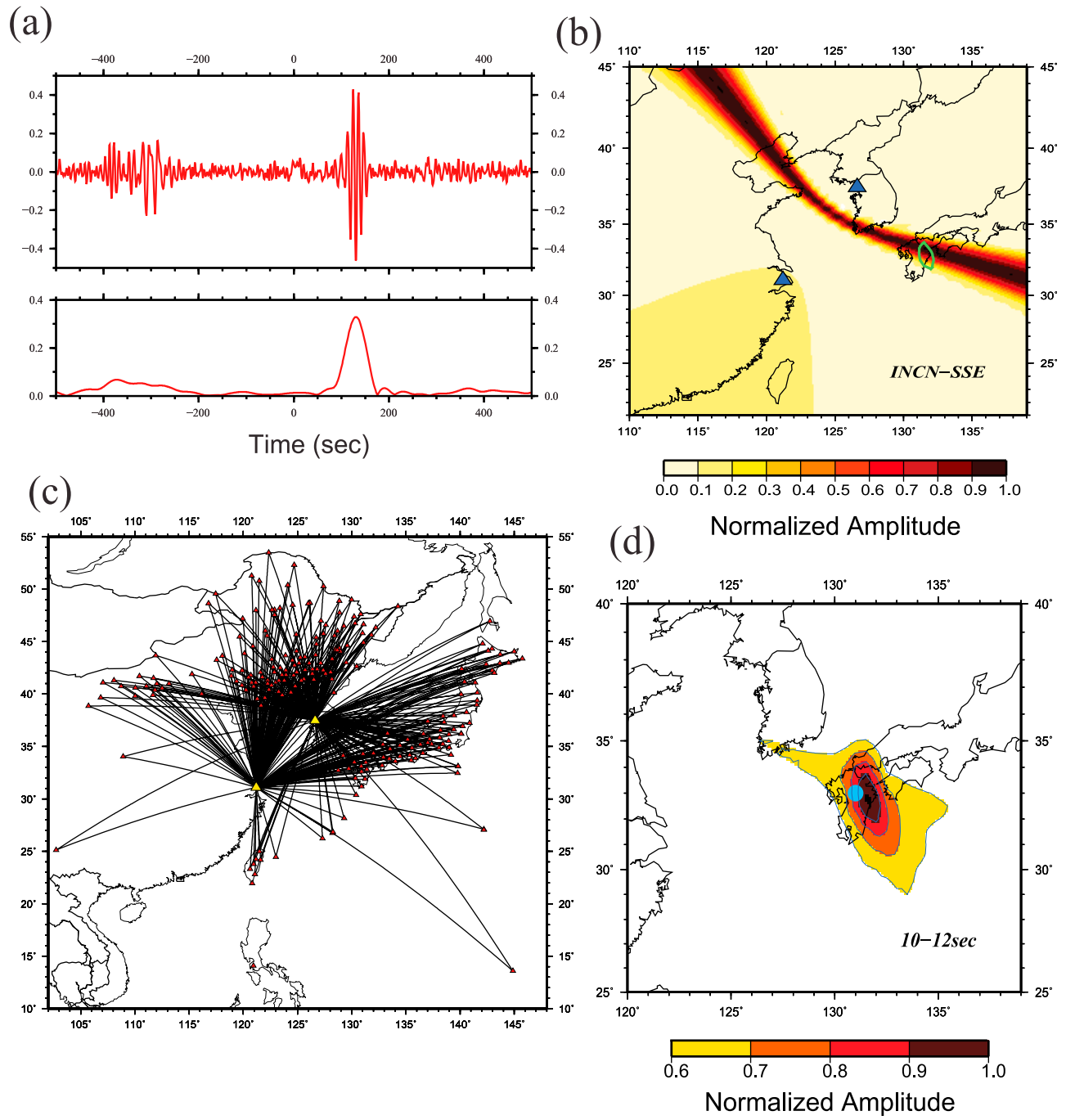

Figure 4. Process to locate the Kyushu microseism. (a) (top) Raw cross correlation (CC) between station SSE and INCN (blue triangles in Figure 4b). (bottom) The envelope function of the CC filtered between 10 and 12 s period. The Kyushu microseismic signal arrives at ~130 s. (b) The migrated hyperbola from the envelope function in Figure 4a, normalized so its maximum value is 1. (c) Paths used to locate the Kyushu microseism are plotted with black lines. We use all paths associated with stations SSE and INCN (yellow triangles). (d) Stack of migrated hyperbolas to locate the Kyushu microseism. Blue circle is the location of *Zeng and Ni* [2010].

wave dispersion on the correlation lag opposite from the arrival of the Kyushu signal in the period band of disturbance. The symmetric component, the average of the cross correlation at positive and negative lag, cannot be used if the Kyushu signal arrives near the interstation Rayleigh wave at either positive or negative correlation lag time.

[22] In practice, we take the following steps. At periods greater than 18 s, we ignore the Kyushu disturbance and use the symmetric component for dispersion measurement. At periods less than or equal to 18 s, the relative arrival time of the Kyushu signal and the surface wave signal at 12 s period guides the measurement. If the expected apparent speed of the

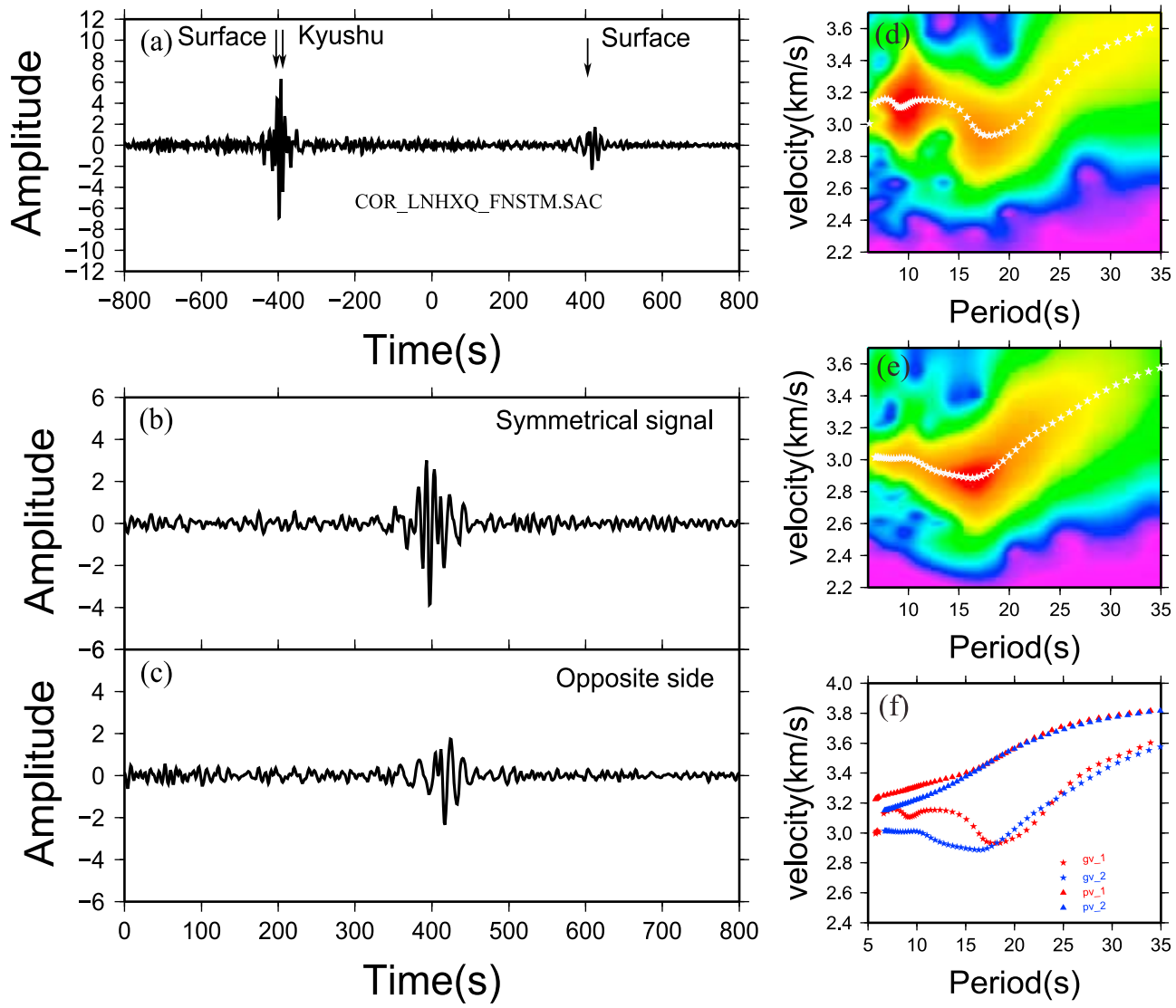

Figure 5. Cross correlations and corresponding frequency-time diagrams illustrating the effect of the persistent Kyushu microseism. (a) Cross correlation between stations HXQ of CEArray and STM of F-Net, where the expected arrival time of the signal from the Kyushu microseism (marked "Kyushu") is close to the arrival time of the surface wave (marked "Surface") on the negative lag component. (b) Example waveform disturbed by the Kyushu microseism: symmetric component cross correlation in which the positive and negative components in Figure 5a are averaged. (c) Example waveform undisturbed by the Kyushu microseism: positive component of the cross correlation in Figure 5a. (d and e) Frequency-time (group velocity) diagrams from Figures 5b and 5c. (f) Comparison between the group velocity curves of cross correlations shown in Figures 5b and 5c. Red triangles and stars are the phase and the group velocity curves from disturbed signal. Blue symbols show the group and phase velocity curves of the undisturbed signal.

Kyushu signal is greater than 4.5 km/s and the length of the interstation path is longer than three wavelengths, then the Kyushu signal is well enough separated from the surface wave that phase and group velocities can be measured on the symmetric component. If the expected apparent speed of the Kyushu signal is less than 4.5 km/s, then we make group and phase velocity measurements on the correlation lag opposite from the Kyushu signal.

[23] As Figure 5a exemplifies, the correlation lag on the opposite side of the Kyushu signal may have a smaller amplitude than the lag containing the Kyushu signal and will have a significantly lower SNR than the symmetric component. Thus, this data processing procedure tends to lower the SNR for many interstation cross correlations between 8 and 16 s period. Because observations are discarded if SNR < 15, this reduces the data set appreciably, as Table 1 shows. We are still left with sufficient high-quality measurements to perform tomography across much of the study region, however.

[24] If left untreated, the Kyushu signal would have vitiated our maps predominantly in South Korea, the southern Sea of Japan, and in the Kyushu region from 8 to 14 s period. Artifacts would have been much stronger on the group velocity than the phase velocity maps. Above 16 s period,

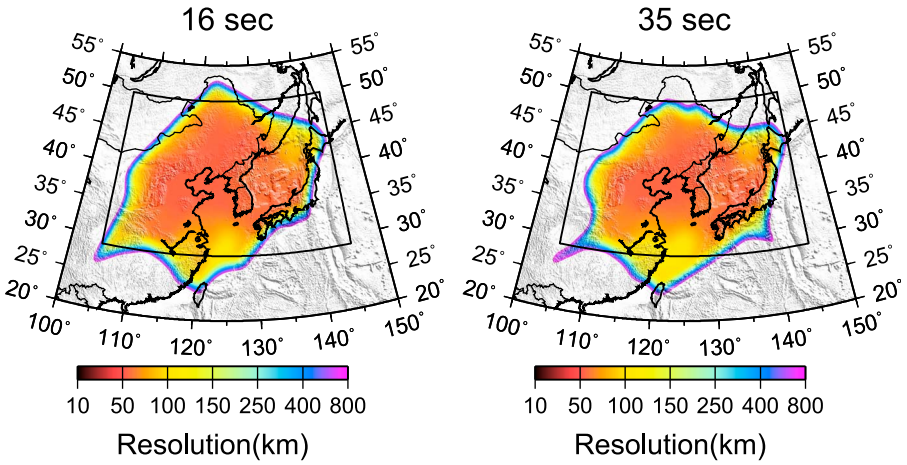

Figure 6. Resolution estimates at periods of 16 and 35 s, presented in units of kilometers and defined as twice the standard deviation of a 2-D Gaussian fit to the resolution surface at each geographic node [*Barmin et al.*, 2001]. The black box shows the region of study.

however, even if left untreated, the Kyushu signal would have had only a weak effect on the estimated maps.

4. Rayleigh Wave Dispersion Maps

4.1. Construction of the Dispersion Maps

[25] Surface wave tomography is applied to the selected dispersion measurements to produce Rayleigh wave group and phase speed maps on a 0.5° × 0.5° grid using the ray theoretic method of *Barmin et al.* [2001]. Being mostly determined over regional (nonteleseismic) interstation distances, the dispersion measurements observed here will not be affected strongly by off–great circle effects [e.g., *Lin et al.*, 2009] except for relatively long paths undergoing a continent-ocean transition. This will primarily affect paths from Japanese F-Net to Chinese stations and the maps of the Sea of Japan may be degraded somewhat by this effect. Finite frequency effects will also be weak in the period band of study [*Lin et al.*, 2011]. The tomographic method of *Barmin et al.* is based on minimizing a penalty functional composed of a linear combination of data misfit, model smoothness, and model amplitude. The choice of the damping parameters is based on the optimization of data misfit and the recovery of coherent model features. Due to a shortage of measurements, we are unable to produce reliable maps below 8 s period and above about 45 s period. The resulting Rayleigh wave dispersion maps, therefore, are constructed between 8 and 45 s on a 2 s period grid.

[26] During tomography, resolution is also estimated via the method described by *Barmin et al.* [2001] with modifications presented by *Levshin et al.* [2005]. Resolution is defined as twice the standard deviation of a 2-D Gaussian fit to the resolution surface at each geographic node. Examples of resolution maps are plotted in Figure 6 for the 16 s and 35 s period measurements. Resolution is estimated to be about 100 km across most of the region of study but degrades to 200–400 km near the boundary of our studied area where station coverage is sparse.

[27] Histograms of data misfit using the dispersion maps at periods of 14 s, 20 s, 30 s, and 40 s are plotted in Figure 7 for phase and group velocity. Group travel time misfits are typically 3–4 times larger than phase travel time misfits because phase velocity measurements are more accurate [*Bensen et al.*, 2007; *Lin et al.*, 2008] and group velocity sensitivity kernels have a larger amplitude. The range of standard deviations of the group travel time misfits runs between about 4 and 5 s and that of phase travel time between about 1 and 1.5 s. Phase travel time misfits of ~1 s between 14 and 30 s period are indicative of the quality of the data set, being similar to misfits that result from USArray data [e.g., *Lin et al.*, 2008].

4.2. Description of the Dispersion Maps

[28] Group and phase velocity maps at periods of 12, 20, 30, and 40 s are plotted in Figures 8 and 9. Only those areas where the spatial resolution is better than 400 km are shown. The 100 km spatial resolution contour is also plotted as a continuous white line. Because the 3-D model is discussed in considerable detail in section 6, discussion of the dispersion maps here is brief but is illuminated by the sensitivity kernels shown in Figure 10. Both phase (solid lines) and group velocity (dashed lines) kernels are shown, computed for 10 and 40 s period at two locations in the final model constructed here: (1) Sea of Japan and (2) North China Craton.

[29] As Figure 10 illustrates, at each period the group velocity measurements are sensitive to shallower structures than the phase velocities. Phase velocity maps, therefore, generally should be compared with somewhat shorter-period group velocity maps. Thus, comparison between Figures 8 and 9 reveals that the phase velocity map at 12 s is similar to the group velocity map at 20 s and the phase velocity map at 20 s is quite like the group velocity pattern at 30 s. Because of the lower uncertainty in the phase velocity measurements, however, the phase velocity maps generally are more accurate than the maps of group velocity.

[30] The dispersion maps are sensitive to quite different structures between short and long periods and between continental and oceanic regions even at the same period as Figure 10 illustrates. The short-period dispersion maps (12 s group and phase velocity in Figures 8 and 9) are primarily sensitive to upper crustal velocities in continental areas, which are dominated by the presence or lack of sediments.

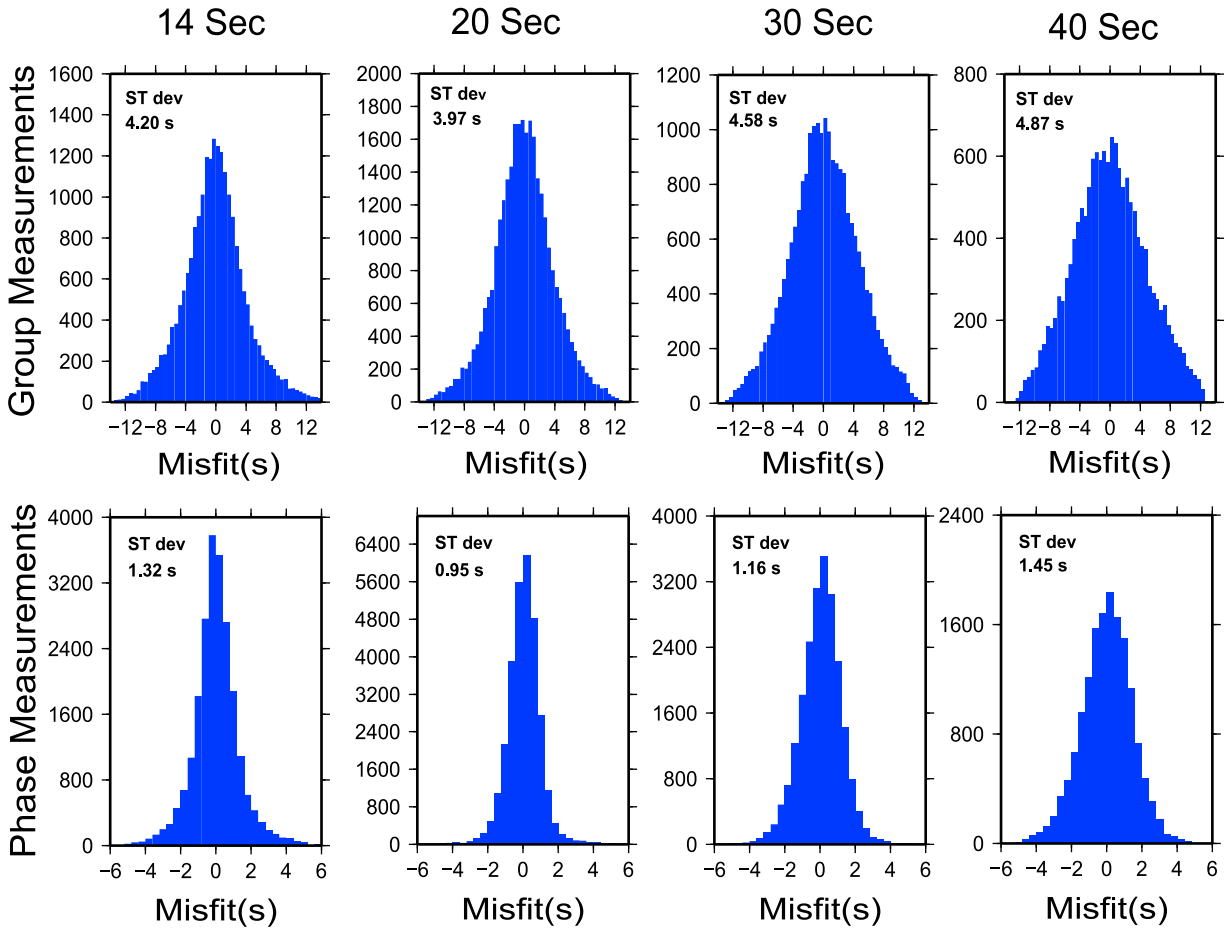

Figure 7. Misfit histograms at periods 14, 20, 30, and 40 s. (top) The group velocity misfit and (bottom) the phase velocity misfits. The standard deviations are shown in each panel.

In regions with oceanic crust, sensitivity is predominantly to uppermost mantle structure. At intermediate periods (20 s phase velocity, 20–40 s group velocity), the maps are mostly sensitive to middle to lower crustal velocities beneath continents and continent-ocean crustal thickness variations. At long periods (30–40 s phase velocity), the maps predominantly reflect crustal thickness variations on the continent and uppermost mantle conditions beneath oceans.

[31] At short periods (12 s), the dispersion maps in Figures 8 and 9 exhibit low-velocity anomalies where sediments are present [*Bassin et al.*, 2000], e.g., the Songliao Basin (SLB), Huabei Basin (HB), Bohai Bay (BH), North China Platform (NC), the Yellow Sea (ESYS), and the Tsushima Basin (TB) in the southern Sea of Japan. The younger, Cenozoic age sediments of Bohai Bay and the Huabei Basin of the North China Craton are much slower than the older, largely Mesozoic age sediments of the Songliao Basin. Higher velocities are imaged in the mountains surrounding the basins, e.g., the Great Xing'an Range (GXAR), Lesser Xing'an Range (LXAR), the Changbai Mountains (CBM), the Yinshan Mountains (YSM), and the Taihang Mountains (THM), which is consistent with the presence of crystalline rocks near the surface. Weak positive anomalies are observed in the Korean Peninsula.

[32] At intermediate periods (20 s phase velocity, 20–30 s group velocity), relatively low wave speeds are still observed for the deeper basins: Songliao, Huabei, Bohai Bay, and Yellow Sea. Group and phase velocity are very high in the Sea of Japan reflecting oceanic mantle lithospheric shear wave speeds that clearly outline the continental boundary of the oceanic crust. It should be noted that off–great circle effects that may exist are not severe enough to distort the borders of the oceanic crust badly. A significant low-velocity anomaly appears in Xing'an–East Mongolia. The anomaly does not develop along the Tancheng-Lujiang Fault, however, but rather to the west of the Songliao Basin, encompassing the Great Xing'an Range and the Yinshan Mountains north of the Ordos Block. To the east of the North-South Gravity Lineament the crust is much thinner than to its west [e.g., *Xu*, 2007].

[33] For group velocity at 40 s and phase velocity at periods of 30–40 s, four principal observations are worth noting. First, the high wave speed anomalies of the Sea of Japan diminish from 30 s to 40 s period on the phase velocity maps. This reflects relatively thin lithosphere beneath the Sea of Japan and increased sensitivity to the underlying asthenosphere by the longer-period waves. Second, the Songliao, Huabei, and Bohai basins are situated within the Songliao-Bohai Graben, which is believed to have formed by back-arc extension and potential rifting [*Liu et al.*, 2001]. This graben, extending from the Songliao Basin into Bohai Bay, is associated with a continuous high-velocity anomaly, which is

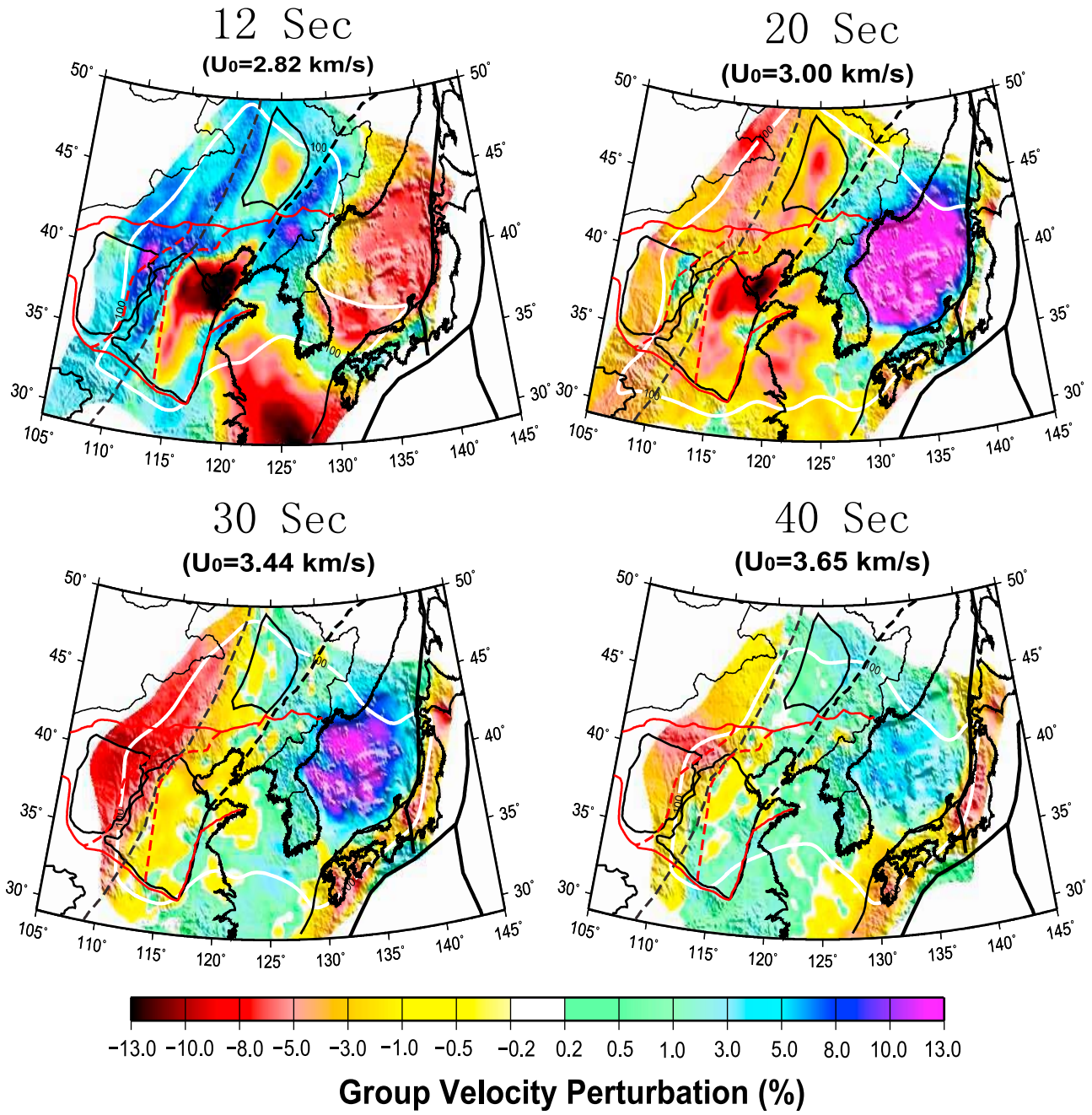

Figure 8. Group velocity maps at periods of 12, 20, 30, and 40 s. Group velocities are plotted as perturbations relative to the average velocity (U_0) within the 400 km resolution contour, and the thick white line is the 100 km resolution contour. Other lines show tectonic and geological boundaries identified in Figure 2.

clearly observable on the 30 and 40 s phase velocity maps. Third, on the longest-period phase velocity maps, low wave speeds are found along the entire length of the Northeast Asia Fold Belt, extending into the Korean Peninsula. Such clear continuous low wave speeds are not apparent on the 40 s group velocity map because of the shallower sensitivity of group velocities than phase velocities. Apparent discrepancies between phase and group velocities such as this one are reconciled by the 3-D Vsv model, as discussed in section 5. Finally, a belt of low velocities is present on the longest-period phase velocity maps in the far eastern Sea of Japan bordering Hokkaido and northern and central Honshu, extinguishing in southern Honshu, and then reinitiating along Kyushu and the Ryukyu Islands.

5. Construction of the 3-D Model

[34] This study is based exclusively on Rayleigh waves, which are primarily sensitive to vertically polarized shear wave speeds (Vsv) that may be slower than horizontally polarized wave speeds (Vsh) in regions where anisotropic minerals are preferentially aligned in the horizontal plane. The velocity difference between Vsv and Vsh is referred to as radial anisotropy. Thus, the model we produce is a Vsv

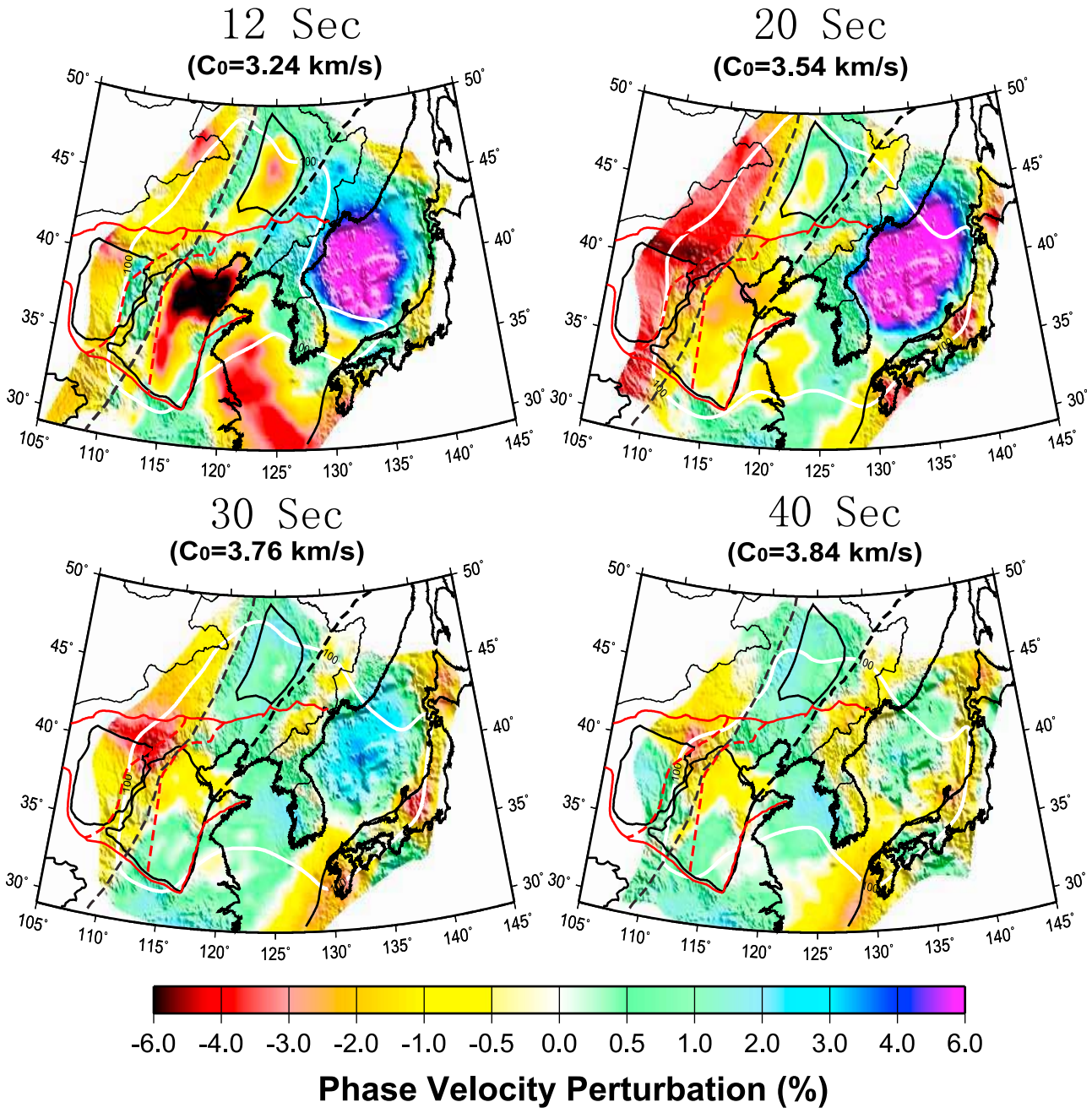

Figure 9. Same as Figure 8 but for phase velocity maps at periods of 12, 20, 30 and 40 s.

model. In the presence of substantial radial anisotropy, Vsv can be several percent lower than the effective isotropic shear wave speed, versus Radial anisotropy is common in both the mantle [e.g., *Ekstrom and Dziewonski*, 1997; *Shapiro and Ritzwoller*, 2002] and the crust [e.g., *Shapiro et al.*, 2004; *Moschetti et al.*, 2010a, 2010b], and is geographically variable. We will generally refer to our 3-D model as being a Vsv model, but for simplicity will also refer to it as a shear wave speed or Vs model.

[35] The 3-D Vsv model is based on the Rayleigh wave phase and group speed maps from 8 to 45 s period on a 0.5° × 0.5° grid across the study region. Periods at which resolution is greater than 200 km are not included in the inversion. This determines the outline of the model and in oceanic regions local dispersion curves typically begin at 12 s period. Local dispersion curves from the eight locations identified with red dots in Figure 2 are shown in Figure 11 with error bars. The group velocity and phase velocity curves shown in Figure 11 are mostly smoothly varying and are able to be fit by a vertically simple Vs model at each point within observational error. In particular, the group and phase velocity curves are reconcilable at each point. Local misfit is presented for each point in Figure 11, where "RMS misfit" means the square root of the reduced chi-square value:

$$\text{RMS misfit} = \left[\frac{1}{N}\sum_i \frac{(d_i - p_i)^2}{\sigma_i^2}\right]^{\frac{1}{2}} \quad (1)$$

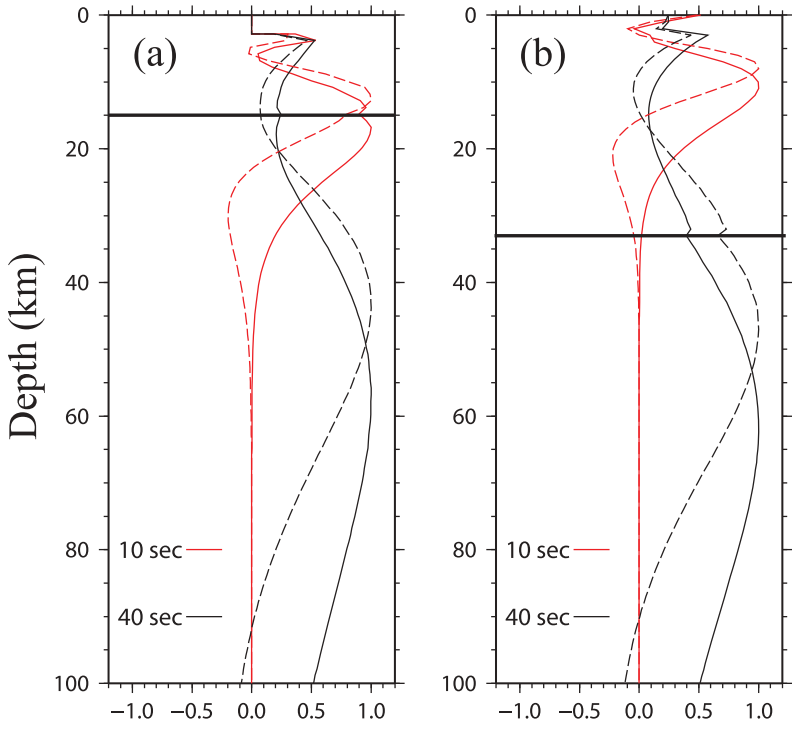

Figure 10. Rayleigh wave phase (solid lines) and group (dashed lines) velocity sensitivity kernels for 10 s (red lines) and 40 s (black lines) periods. (a) Kernels are based on our 3-D model in the Sea of Japan (point H, Figure 2). (b) Kernels are based on our 3-D model in the North China Craton (point B, Figure 2). The horizontal black lines denote local Moho depth at each point.

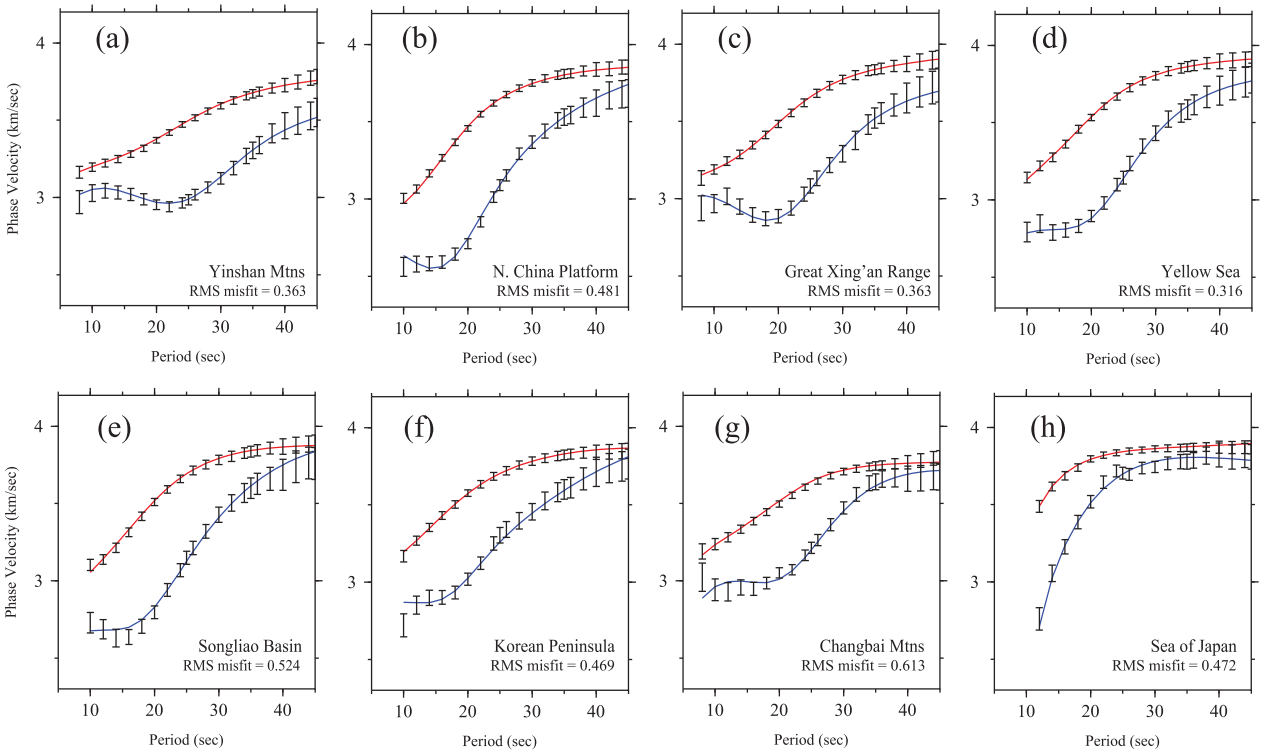

Figure 11. (a–h) Phase and group velocity observations at the eight locations identified with letters in Figure 2, presented with error bars intended to be 1σ. The dispersion curves are predicted by the center of the ensemble of models shown in Figure 12 for each location, with red lines being phase velocity and blue lines group velocity. The RMS misfits are calculated by equation (1).

where d_i is the observed group or phase velocity value, p_i is the value predicted from the model, σ_i is the uncertainty for the observation, and N is the total number of phase plus group velocity values along the dispersion curves.

[36] Uncertainties in phase and group velocity curves are notoriously difficult to determine reliably, as they are typically underestimated by most tomographic codes based on standard error propagation [e.g., *Barmin et al.*, 2001]. They can be estimated reliably by using the eikonal tomography method [*Lin et al.*, 2009], but the method requires more uniform array spacing than exists in the study region. Therefore, the uncertainties shown in Figure 11 are not from the data set presented here, but, as discussed in section 2, misfit statistics in the present study are similar to those that emerge in the western U.S. based on the regularly spaced USArray Transportable Array. For this reason, we take the average uncertainties estimated by eikonal tomography using USArray in the western U.S., but to be conservative we double them [*Lin et al.*, 2009; *Moschetti et al.*, 2010a, 2010b].

[37] The 3-D model is constructed via a Monte Carlo method that is similar to the methods of *Shapiro and Ritzwoller* [2002] and *Yang et al.* [2008a, 2008b]. The starting model for the Monte Carlo search derives from the Vsv values of the global model of *Shapiro and Ritzwoller* [2002] with two principal modifications. First, we simplify the starting crustal model considerably: the two sedimentary layers and three crystalline crustal layers of the model of Shapiro and Ritzwoller are averaged separately to define only two constant velocity layers (not including a possible water layer). Second, crustal thickness is not allowed to be less than 20 km in the Sea of Japan, as discussed in section 6.1. Uniformly distributed perturbations in Vsv are considered using a single sedimentary layer with variable thickness and shear velocity, four B-splines for Vsv in the crystalline crust, and five B-splines in the mantle to a depth of 150 km, below which the model is a constant velocity half-space. The resulting model is vertically smooth in both the crystalline crust and mantle. Moho depth is allowed to vary in a uniform interval of ±10 km relative to the starting model. Vsv is constrained to increase monotonically in the crystalline crust and the depth derivative of velocity directly below Moho is constrained to be positive (i.e., velocity increases with depth right below Moho, but can decrease deeper into the mantle). Both constraints are introduced to reduce the model space, in particular the magnitude of the trade-off between Moho depth with structures at depths adjacent to Moho. The positivity constraint on the depth derivative of velocity in the uppermost mantle typically introduces a thin low velocity "sill" right below Moho, which is an artifact of the constraint.

[38] The model has no radial anisotropy, thus Vs = Vsh = Vsv. Also, we assume that the crystalline crust and mantle is a Poisson solid and set Vp = 1.73Vs, in the sediments we use Vp = 2.0Vs, and for density we use the scaling relation advocated by *Christensen and Mooney* [1995]: $\rho = 0.541 + 0.3601$Vp, where ρ is in g/cm^3 and Vp is in km/s. We apply a physical dispersion correction [*Kanamori and Anderson*, 1977] using the Q model from PREM [*Dziewonski and Anderson*, 1981], and the resulting model is reduced to 1 s period. Offshore, the water depth is recalculated based on a $0.2° \times 0.2°$ average of bathymetry at each point.

[39] Models are chosen randomly guided by a Metropolis algorithm [e.g., *Mosegaard and Tarantola*, 1995] and are accepted if the reduced χ^2 misfit to the dispersion curves is less than twice the minimum misfit, $\chi^2_{\min}$, at each location. Reduced χ^2 misfit is the square of RMS misfit defined by equation (1). RMS misfit averages less than 1.0 across the region of study. Much of this misfit results from group velocities at short periods.

[40] As examples, the procedure yields the eight ensembles of models presented in Figure 12 derived from the eight pairs of Rayleigh wave dispersion curves shown in Figure 11. The ensemble is represented by the gray shaded region, which presents two standard deviations (2σ) around the mean at each depth in each direction. The dispersion curves predicted by the best fitting model are shown in Figure 11 as the blue (group velocity) and red (phase velocity) lines. At each depth, the Vsv model that we plot in subsequent figures and its uncertainty are defined by the middle and one standard deviation of the ensemble, respectively. The quarter width of the ensemble is approximately one standard deviation (1σ). The uncertainties in the model are largest where shear wave speeds trade-off effectively with boundary topography, which occurs near free boundaries in the model: Moho and the base of the sedimentary layer. Thus, uncertainties typically grow near the top of the crystalline crust and both above and below Moho.

[41] The eight examples of dispersion curves and the ensembles of models that fit them, presented in Figures 11 and 12, demonstrate how vertically smooth models with two discontinuities can fit the data well across the study region. A closer inspection of the model profiles, however, reveals the limitations of inversion methods based exclusively on surface waves. In particular, the model is affected by the starting model around which the Monte Carlo method samples, particularly sedimentary thickness and crustal thickness.

[42] On the continent, input model dependence is most important beneath sedimentary basins where our simple parameterization of sedimentary velocities may not faithfully represent local structure. A potential example of this is shown in Figure 12e, beneath the Songliao Basin. Model velocities beneath the basin are very low (~3.2 km/s) in the crystalline upper crust, which causes a large vertical crustal velocity gradient that may not be realistic. Thus, errors in the input model and the simplicity of parameterization of sedimentary structure may bias Vs low in the upper crystalline crust. For this reason, we do not interpret the resulting 3-D model at depths above the lower crust. Imposition of constraints from receiver functions would help to resolve this issue, but is beyond the scope of this work.

[43] In the ocean, in contrast, crustal thickness in the starting model is more poorly known than on the continent. Surprisingly, however, the resulting model is fairly independent of the starting model. This is illustrated by Figure 13, which shows the resulting ensemble of models for a point in the Sea of Japan with two different starting models in which Moho is at 8 km (Figure 13a) or 20 km (Figure 13b), respectively. In both cases the surface wave data are fit admirably and nearly identically (e.g., Figure 12h). With different starting Moho depths of 8 km and 20 km, estimated mantle velocities at 20 km depth are nearly identical in the two ensembles. Crustal velocities and crustal thicknesses differ somewhat (average is 13 km and 15 km, respectively), but are within estimated error. Although crustal thickness

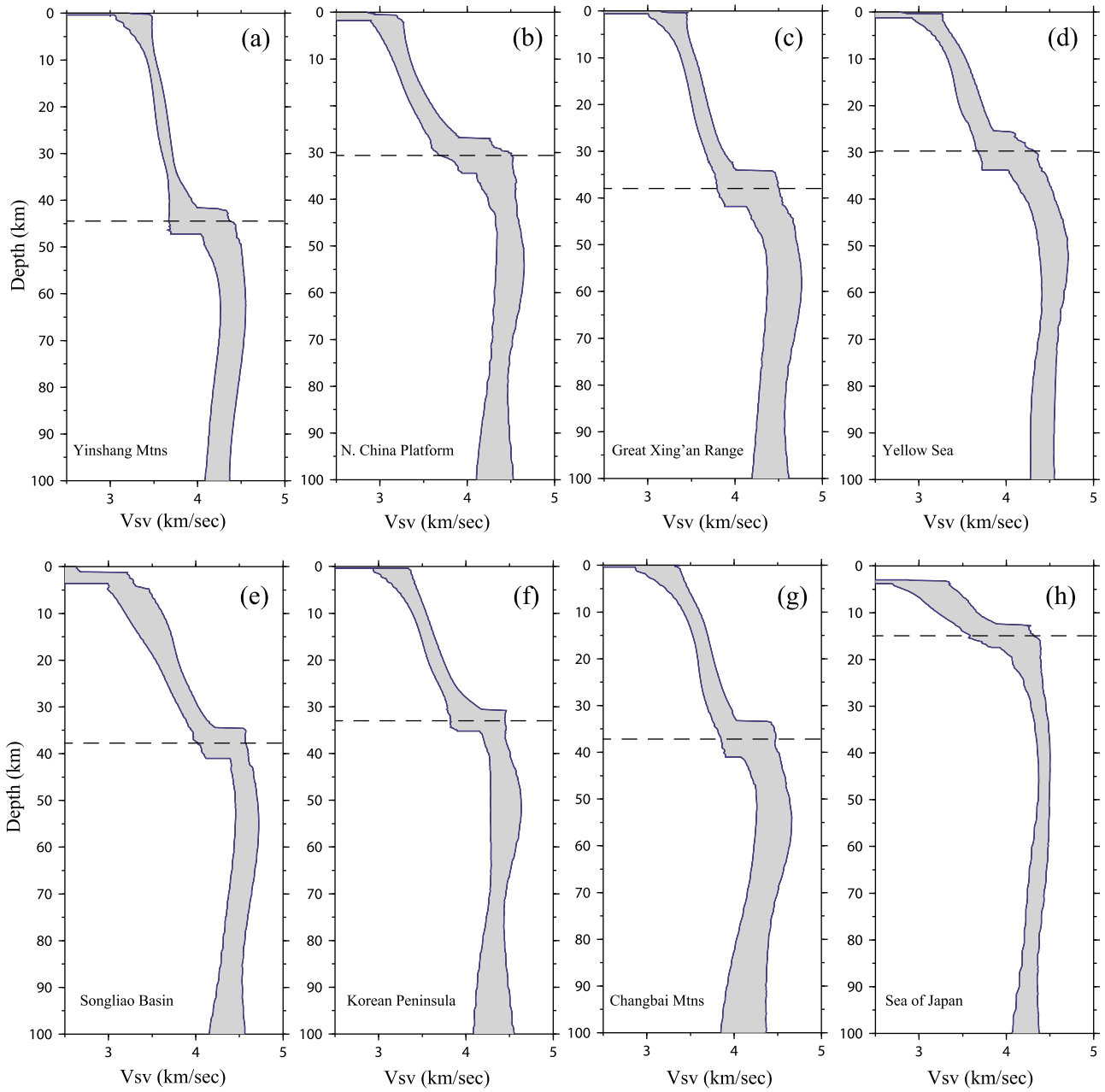

Figure 12. (a–h) Shear wave (V_{sv}) velocity profiles at the eight selected locations identified with letters in Figure 2 constructed to fit the corresponding dispersion curves shown in Figure 11. The gray corridor is the 2σ (standard deviation) uncertainty, and the dashed lines indicate Moho depth.

may vary from 10 km [*Sato et al.*, 2004] to more than 20 km [*Kurashimo et al.*, 1996] across the Sea of Japan, by setting the starting Moho depth to 20 km we are able to estimate mantle velocities reliably and recover crustal velocities and thicknesses to within estimated errors. Further discussion of crustal thickness beneath the Sea of Japan is presented in section 6.2, which describes the observed anticorrelation between crustal thickness and seafloor depth and provides further support for the argument that crustal thickness is relatively well determined beneath the area.

[44] A terminological issue may require clarification. By "crustal thickness" we mean the thickness of the crust including surface topography and a water layer if it exists. By "Moho depth, " we mean the depth to Moho below the geoid. By "solid crustal thickness" we refer to the thickness of the crust not including a water layer.

[45] Results from the individual vertical profiles are aggregated into the 3-D model: the middle of the ensemble of accepted models defines the model profile at each point and the spread at each depth yields the uncertainty. Figure 14 shows the Vsv model at four depths: in the lower crust at 80% of the depth to Moho (Figure 14a), 40 km (Figure 14b), 60 km (Figure 14c), and 80 km (Figure 14d) beneath the surface. Because the dispersion curves extend only up to 45 s period, the model is not reliable beyond a depth of ~100 km. Estimated Moho depth and its uncertainty are shown in

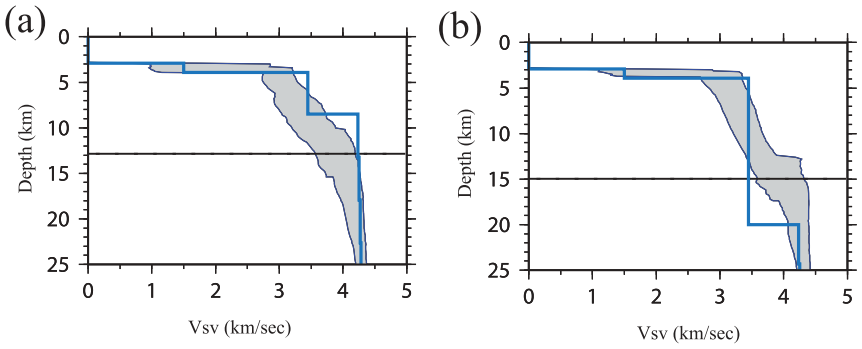

Figure 13. Comparison between inversions performed in the Sea of Japan (point H, Figure 2) using data from Figure 11h with two starting models identified with blue lines: (a) Moho at 8 km and (b) Moho at 20 km. Horizontal lines mark the median Moho depths. The resulting ensembles of models are quite similar, with differences within model uncertainties.

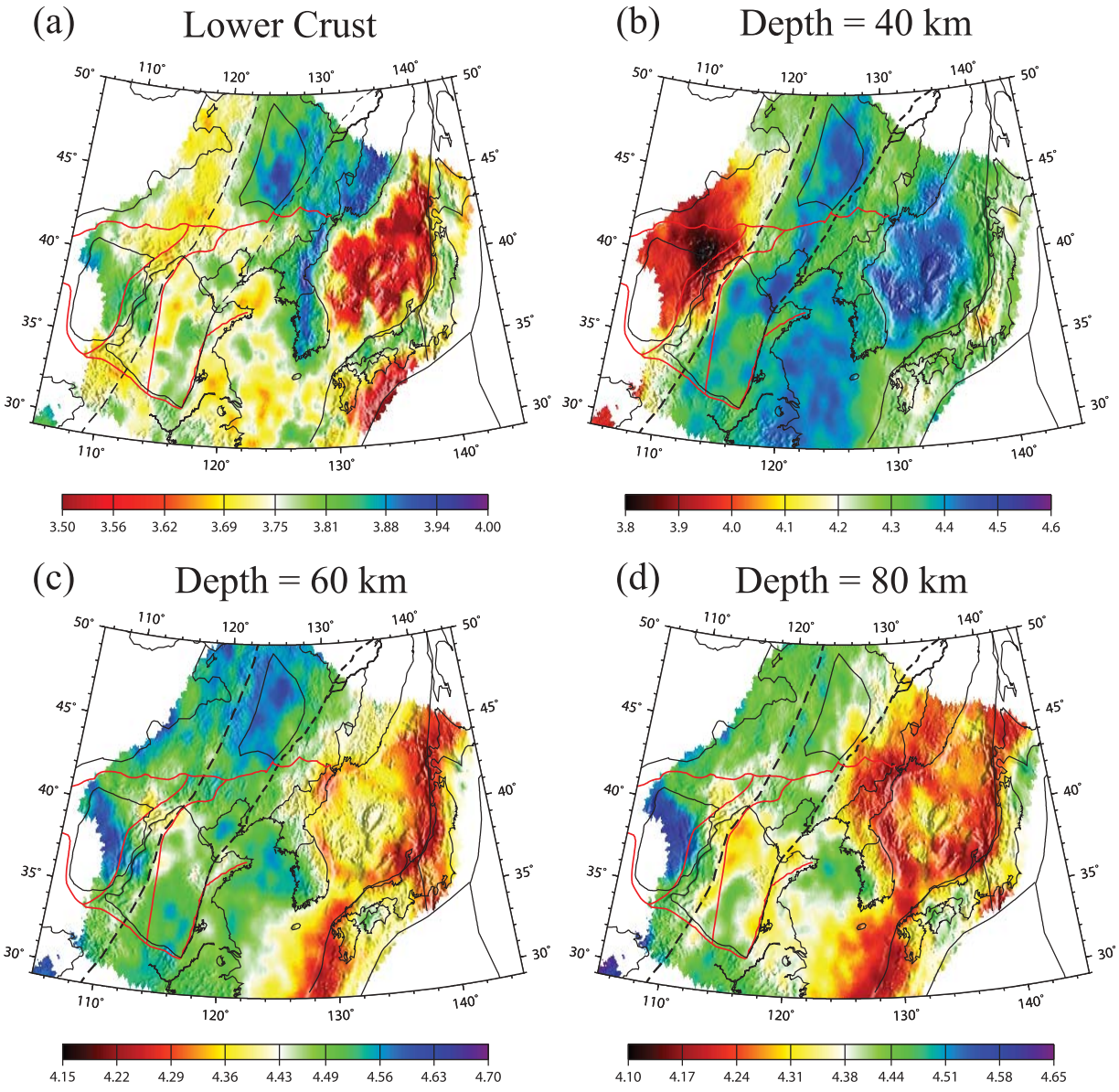

Figure 14. Four horizontal depth slices through the 3-D Vsv model: (a) in the lower crust at a depth of 80% of Moho depth, (b) 40 km, (c) 60 km, and (d) 80 km depth. Color bars beneath each panel give the range of shear wave speeds in km/s.

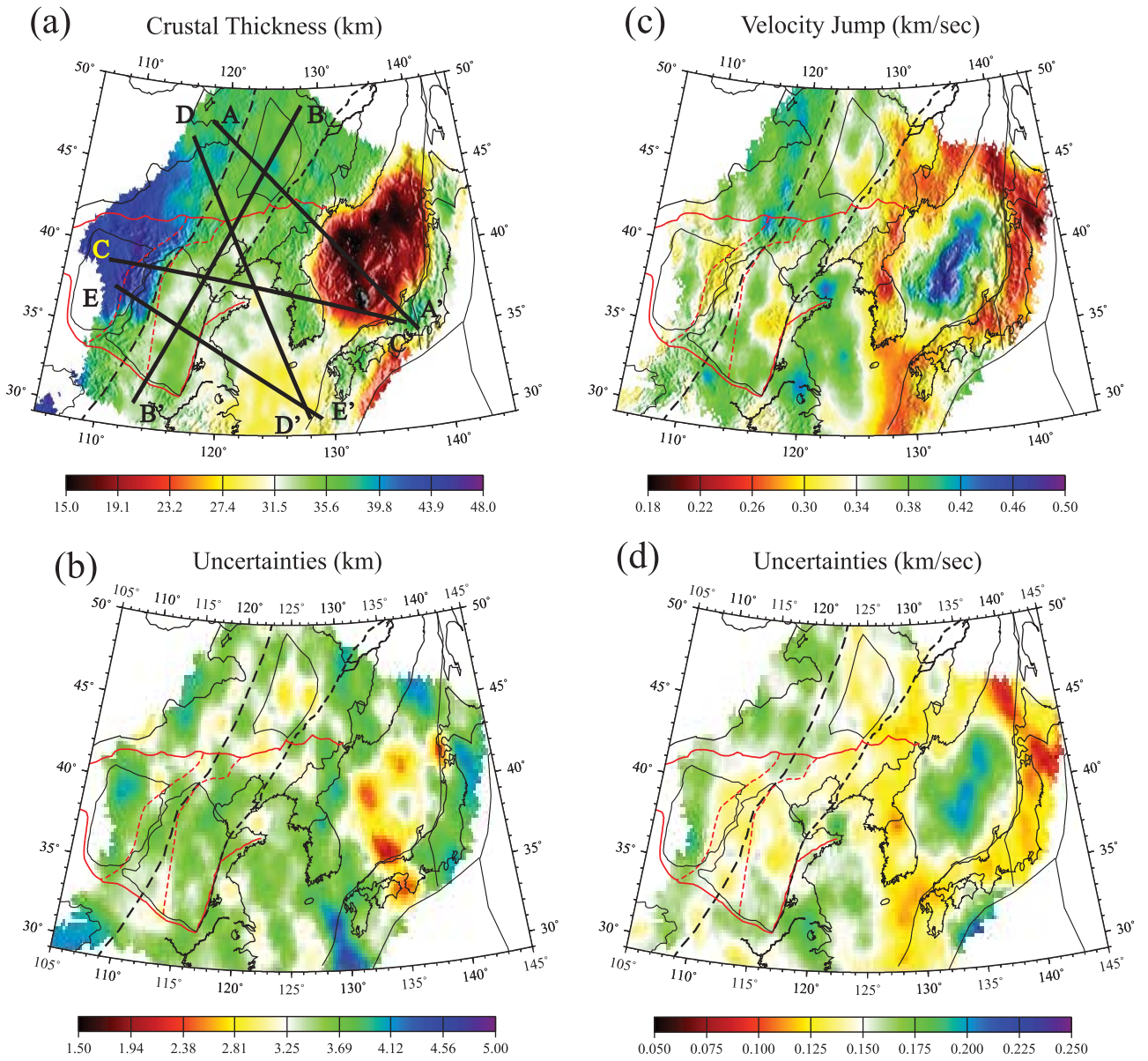

Figure 15. (a) Estimated crustal thickness and (b) 1σ uncertainty in crustal thickness, both in kilometers. The lines A-A′, B-B′, etc. in Figure 15a are the locations of the vertical profiles shown in Figure 17. (c) Shear velocity jump across Moho (km/s) and (d) 1σ uncertainty in the shear velocity jump across Moho, also in km/s.

Figure 15. Figure 15 also presents the estimated velocity jump across Moho and its uncertainty. Uncertainties in shear wave speed at the four depths shown in Figure 14 are presented in Figure 16. Five vertical slices of the model are presented in Figure 17 along the profiles identified in Figure 15a: A-A′ extending northwest-southeast through the Songliao Basin and the Sea of Japan, B-B′ running northeast-southwest through the Songliao Basin and the eastern North China Craton, C-C′ extending roughly west-east from the Ordos Block through the North China Craton, the Bohai Gulf, Korean Peninsula, and the southern Sea of Japan, D-D′ running northwest-southeast from Xing'an–East Mongolia through the Yellow Sea to the East China Sea, and E-E' extending northwest-southeast from the Ordos Block, through the eastern NCC, to the East China Sea. The model is discussed in detail in section 6.

[46] Model uncertainties are presented in Figure 15b for Moho and in Figure 16 corresponding to the horizontal depth slices in Figure 14. Model uncertainties are largest near Moho, i.e., in the lower crust and uppermost mantle as Figures 16a and 16b reflect. At 40 km depth, large uncertainties follow the North-South Gravity Lineament, which marks the point at which Moho depth approximately crosses 40 km. Uncertainties at 40 km are smallest in the Sea of Japan because the crust is thinnest and this depth is most distant from Moho. Uncertainties diminish as one moves deeper beneath Moho, but grow again in the deeper parts of the model as data constraints weaken (Figures 16c and 16d).

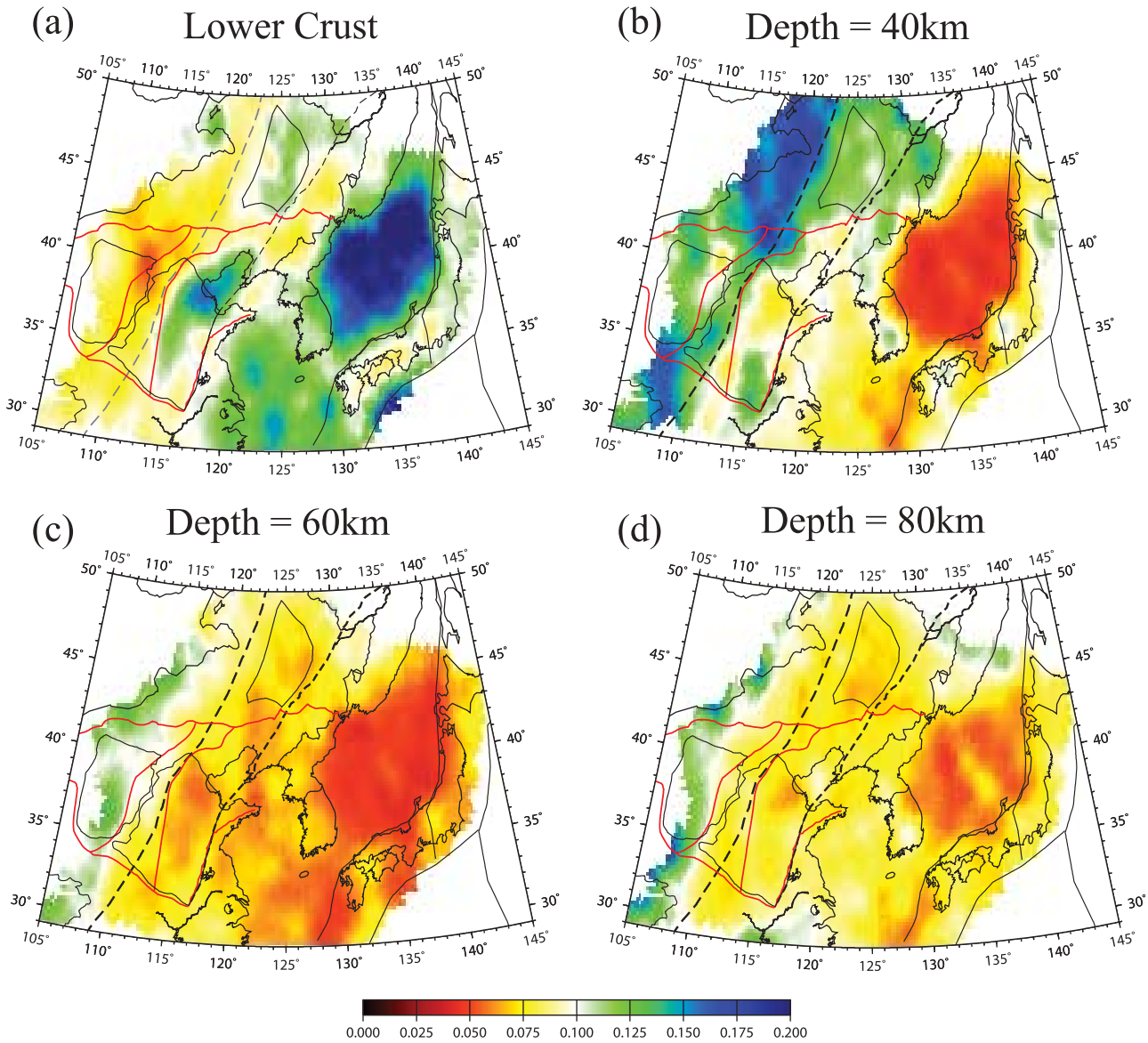

Figure 16. (a–d) Uncertainty (1σ) in Vsv at the four depths shown in Figure 14. Uncertainties are in km/s.

Uncertainties in crustal thickness are nearly homogeneous across the study region, but diminish somewhat beneath the Sea of Japan. Conversely, uncertainties in the velocity jump across Moho are largest beneath the Sea of Japan.

6. Discussion

6.1. Structural Features of the 3-D Model

[47] As discussed in section 5, the trade-off between sedimentary thickness and shear velocities in the upper crust is strong beneath the Songliao and Huabei Basins; thus, we do not present or discuss upper crustal velocities here. Lower crustal velocities are much more robust, however, and they are shown in Figure 14a, which is a profile taken at 80% of the Moho depth. On the continent, lower crustal velocities average about 3.75 km/s, but bifurcate. Velocities are higher, averaging about 3.90 km/s, beneath the Korean peninsula, the Northeast Asian Fold Belt and the Songliao Basin but are slower elsewhere, including the North China Craton, the Xing'an–East Mongolia, and the Yellow Sea, averaging about 3.80 km/s. The high-velocity lower crust beneath far eastern Asia and the Songliao Basin may represent compositional differences between these regions and the tectonically distinct North China Craton and Xing'an–East Mongolia. The slowest lower crustal velocities are observed beneath the Sea of Japan, running between about 3.50 to 3.60 km/s. The largest uncertainties in lower crustal velocities are for the Sea of Japan, however (Figure 16a).

[48] We use the term "mantle lithosphere" here qualitatively and relatively, and it may be substituted with the term "seismic lid. " We take it to mean the high-velocity zone in the uppermost mantle more or less directly below Moho. Thus, in our usage, the base of the lithosphere is the depth at which velocities begin to decrease beneath a higher-velocity overriding mantle. With this definition, on the vertical profiles in Figure 17 the base of the lithosphere occurs at

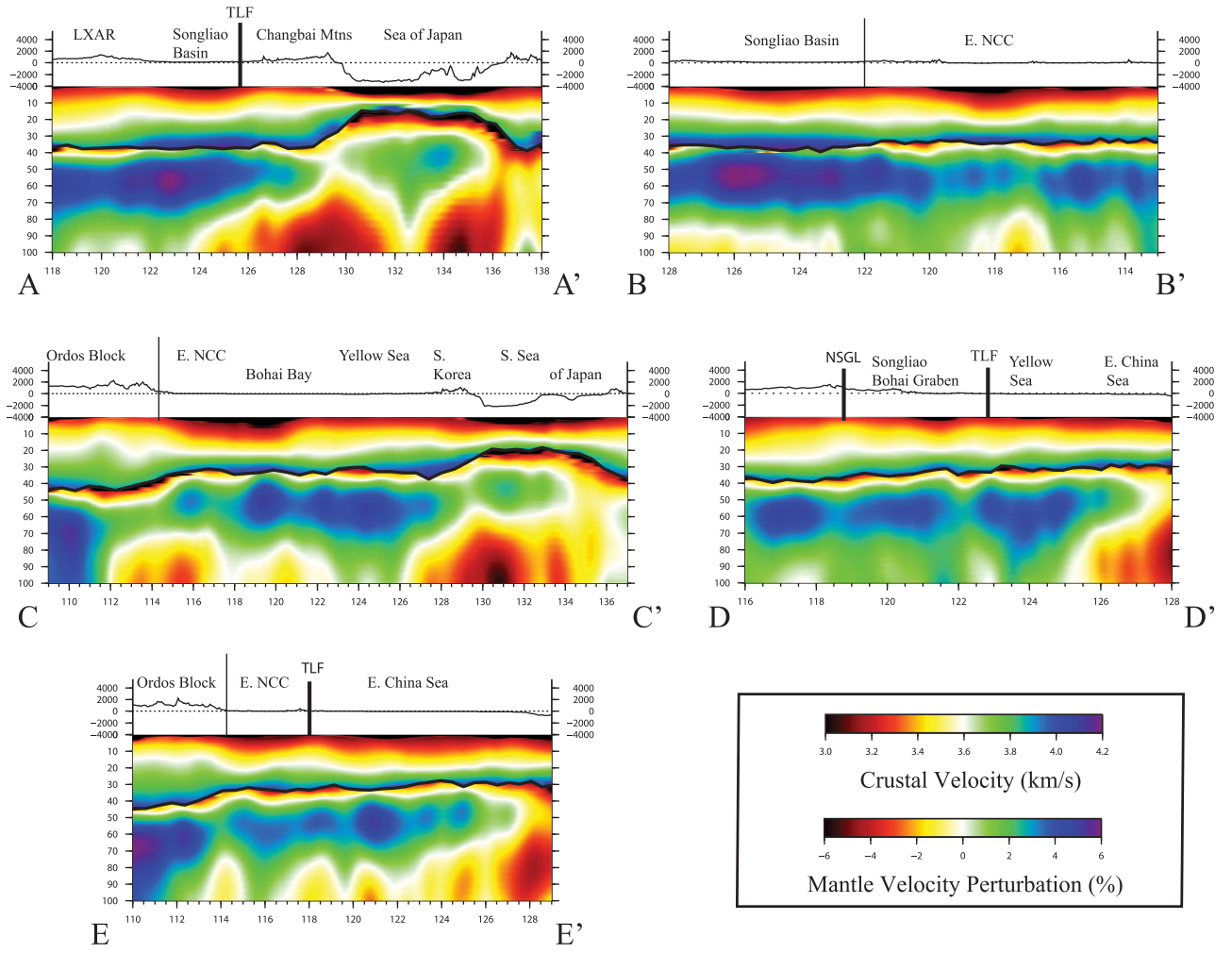

Figure 17. Five vertical profiles through the 3-D model along the lines shown in Figure 15a. Crustal velocities are presented using an absolute scale, and mantle velocities are defined relative to 4.35 km/s.

the depth at which blue colors give way to green colors (~4.5 km/s) if the highest velocities are blues. If the highest velocities are greens (e.g., beneath the Sea of Japan), the base of the lithosphere occurs where the greens give way to white (~4.4 km/s). The term "asthenosphere" is defined more quantitatively, as the region of the mantle where Vs < 4.25 km/s, or where red colors are found in Figure 17. With these definitions, for example, the lithosphere is 70–80 km thick beneath the Songliao Basin (Figure 17, profile B-B′) and is 50–60 km thick beneath the Sea of Japan (Figure 17, profile A-A′). The asthenosphere exists on the vertical profiles only beneath some of the North China Craton (Figure 17, profiles B-B′ and C-C′), the regions bordering the Sea of Japan (Figure 17, profiles A-A′ and C-C′), and the East China Sea (Figure 17, profiles D-D′ and E-E′). Thus, with these definitions, across most of the region the asthenosphere is not reached by 100 km depth. Across most of the region the lithosphere is underlain by a zone that is transitional between lithospheric and asthenospheric, which appears mainly as green and yellow colors on the vertical profiles.

[49] In terms of deeper structures, we describe four principal features: (1) crustal thickness variations across the region, (2) the lithospheric structure of the Songliao – Bohai graben, (3) the uppermost mantle beneath the Sea of Japan and the East China Sea, and (4) the uppermost mantle beneath the North China Craton.

[50] 1. Crustal thickness is presented in Figure 15a. Although internal boundaries such as Moho are notoriously difficult to estimate reliably from surface waves, particularly beneath continents, crustal thickness is about 40 km along the North-South Gravity Lineament (NSGL). The region west of the North-South Gravity Lineament is in the crust at 40 km depth, whereas 40 km lies in the mantle beneath the rest of the region. Thus, the lowest velocities near the western edge of the map in Figure 14b simply reflect crustal wave speeds. Beneath the Sea of Japan, as Figure 13 illustrates, the ability to estimate crustal thickness improves relative to the continent. A blowup of the crustal thickness is presented in Figure 18a. As expected, the crust is thinnest where the sea is deepest, principally in the Japan Basin, which defines the northern and western parts of the Sea of Japan. The crust thickens, for example, beneath the Yamato Rise, the topographic rise in the central Sea of Japan. Crustal thickness beneath the Sea of Japan is discussed further in section 6.2,

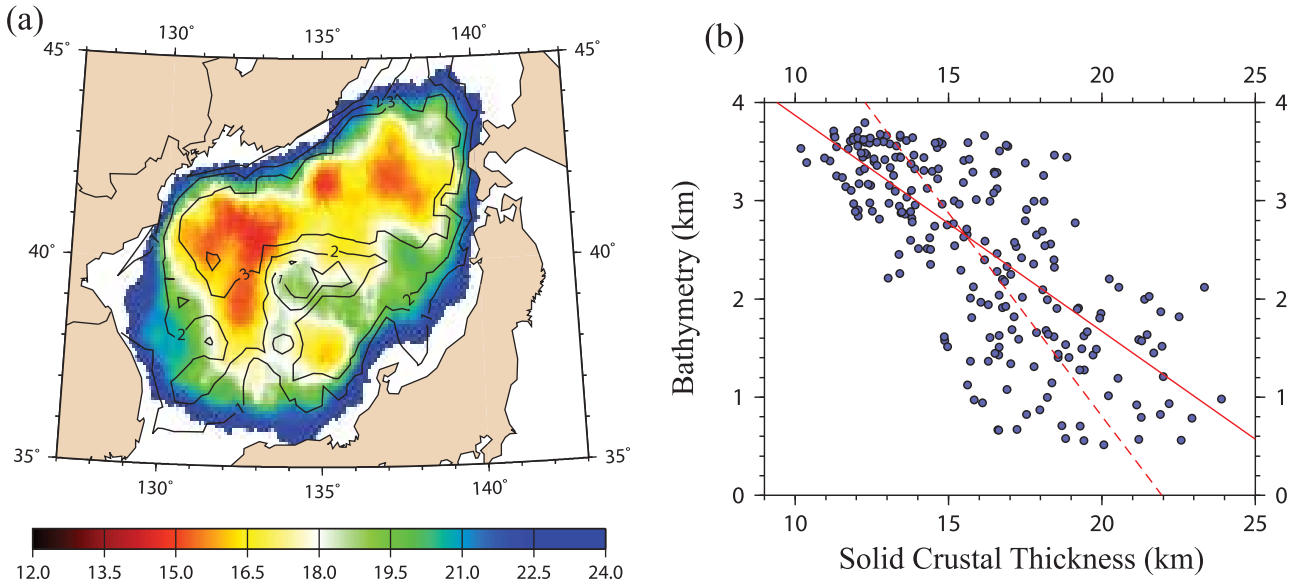

Figure 18. (a) Blowup of part of Figure 15a, showing crustal thickness across the Sea of Japan (in kilometers). Contours of bathymetry are overplotted in increments of 1 km to illustrate the anticorrelation between crustal thickness and seafloor depth. (b) Plot of seafloor depth versus solid crustal thickness (crustal thickness minus ocean depth) with values on a 0.5° × 0.5° grid across the Sea of Japan shown as blue dots. The solid red line is the least squares fit line in which seafloor depth is the dependent variable, and the dashed red line is the fit in which crustal thickness is the dependent variable.

where the anticorrelation observed between crustal thickness and water depth is used to support the reliability of the crustal thickness estimates in oceanic regions.

[51] 2. At 40 km depth east of the North-South Gravity Lineament relatively high wave speeds (>4.4 km/s) lie beneath the Songliao Basin and run to the Bohai Sea, as Figure 14b shows. The high velocities beneath the Songliao Basin form a lid that extends to 60–70 km but then terminates, being underlain by more normal continental uppermost mantle wave speeds beneath the Basin by 80 km depth. This can be seen clearly on vertical profiles A-A′ and B-B′ of Figure 17, in which the relatively thick fast lithosphere beneath the Songliao graben is contrasted with the thinner slower lithosphere of the North China Craton and the Sea of Japan. The mantle lithosphere, however, beneath the Songliao Basin is not cratonic in nature, contrasting with the much thicker lithosphere beneath the Ordos Block (e.g., Figure 14d). Although the Ordos Block is only partially imaged in this study, high velocities are seen to underlie it in the uppermost mantle extending at least to 100 km depth (and presumably deeper) as vertical profile C-C′ in Figure 17 illustrates. Although the lithosphere underlying the Songliao Basin is not as thin as beneath the North China Craton, it is thin for a region believed to have a basement of Archean age.

[52] 3. At 40 km depth, relatively high wave speeds (>4.4 km/s) also underlie the Yellow and Japan Seas. Although similar in the uppermost mantle, below 40 km the mantle structures beneath these seas lose their similarity. The uppermost mantle beneath the Yellow Sea is continental in character as profile D-D′ in Figure 17 shows. Much lower wave speeds exist in the back-arc spreading region beneath the Sea of Japan, as can been seen on Figures 14c and 14d. Starting at about 60 km depth, low velocities bound the eastern margin of the Sea of Japan and also to a somewhat lesser extent the western margin, extending onto the continent. Low velocities also bound the eastern edge of the East China Sea, east and southeast of the Yellow Sea near the Ryukyu Islands. By 80 km depth, the bifurcated low-velocity zone across the Sea of Japan has largely merged into a more homogeneous low-velocity asthenosphere beneath the entire sea, and the western edge of the anomaly has spread further inland to underlie the Northeast Asia Fold Belt, including the volcanic region of the Changbai Mountains. This is presented most clearly in Figure 19, which displays two low-velocity contours at 80 km depth: Vs < 4.25 km/s and 4.25 km/s ≤ Vs < 4.35 km/s. This also can be seen clearly in profile A-A′ of Figure 17, which extends across the center of the Sea of Japan, but is also visible in profile C-C′ which run through the sea farther south. We refer to the low velocities bounding the Sea of Japan as a "Y-shaped" anomaly on vertical profiles, which is apparent on profile A-A′. A relatively high velocity 50–60 km thick lithosphere is observed beneath the central Sea of Japan, as profiles A-A′ and C-C′ illustrate. This relatively thin lithosphere should be contrasted with the thicker faster lithosphere beneath the Songliao Basin, which is clearly seen on profile A-A′. The bordering Y-shaped asthenospheric anomaly and the thin lithosphere underlying the Sea of Japan are discussed further in section 6.3. The East China Sea lies near the southeastern corner of our study region, but like the Sea of Japan its eastern margin near the Ryukyu Islands is underlain by low velocities in the uppermost mantle. This is apparent in Figures 19 and 14d and vertical profile D-D′ in Figure 17. Unlike the Sea of Japan, however, there is no "Y-shaped" anomaly beneath the East China Sea as the western part of the sea merges with fast continental lithosphere beneath the Yellow Sea with no low-velocity feature in the uppermost mantle.

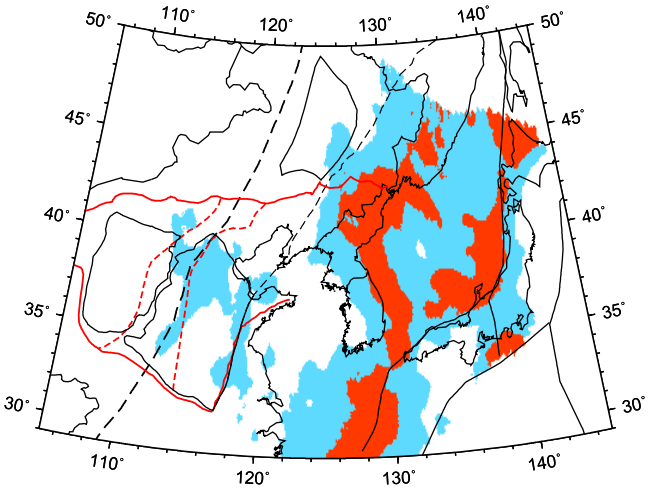

Figure 19. Simplified representation of the 3-D model in the upper mantle, showing the distribution of low velocities at 80 km depth with velocity intervals: red, Vsv ≤ 4.25 km/s; blue, 4.25 < Vsv ≤ 4.35 km/s. The red contour identifies the "Y-shaped" anomaly that underlies the Sea of Japan and parts of northeastern Asia believed to arise from slab dehydration at several depths overlying the stagnant slab. The blue region surrounding the red contour is the large area of the uppermost mantle affected by back-arc spreading. The blue contour within the North China Craton identifies the "horseshoe" shaped anomaly that flanks the eastern North China Craton, believed to result from intense tectonothermal modification that may have reached as high as the base of the crust.

[53] 4. The North China Craton deviates from most of the rest of continental northern and northeastern China by possessing much slower wave speeds at depths greater than about 60 km. This can be seen clearly on profile B-B′ of Figure 17, which shows that the mantle lithosphere beneath the North China craton is thinner and slower than beneath the Songliao Basin. Profile C-C′ illustrates, however, that the lithosphere extends deeper than beneath the Sea of Japan, with underlying asthenosphere that is not as slow. However, asthenospheric wave speeds do underlie the lithosphere beneath the North China Craton below about 80 km depth. These low wave speeds in the uppermost mantle are horseshoe in shape on horizontal cross sections across the eastern North China Craton as seen in Figure 19, in which the low velocities follow the western and eastern flanks of the eastern part of the North China Craton. The middle of the eastern part of the North China Craton is not slow, however. The seismic structure of the North China Craton is discussed further in section 6.4.

6.2. Seafloor Depth and Crustal Thickness Beneath the Sea of Japan

[54] The crustal structure beneath the Sea of Japan is highly heterogeneous [e.g., *Taira*, 2001]. The Japan Basin is principally oceanic crust, while most of the Yamamoto and Tsushima basins are extended continental crust, the Korean Plateau and Yamamoto Rise are composed mainly of continental crust, and the eastern and southern boundaries of the Sea are rifted continental crust [*Tamaki et al.*, 1992]. Thus, crustal thickness varies appreciably across the basin in a way that we expect to be related to seafloor depth, assuming isostatic compensation. Figure 18b presents seafloor depth (bathymetry) across the Sea of Japan plotted versus solid crustal thickness from our 3-D model. Seafloor depth and our estimate of crustal thickness (Figure 18a) are correlated, although there is substantial scatter. Assuming that water depth, H_W, is the dependent variable and solid crustal thickness, H_C, is the independent variable, the least squares linear fit, shown as the solid red line in Figure 18b, is $H_W = -0.22\ H_C + 6.07$, where H_W, H_C, and the constant term are in km. The linear fit provides a variance reduction of 57%.

[55] The observed derivative $dH_W/dH_C = -0.22$ provides information about the nature of isostatic compensation in the region. For crustal Airy isostasy, with mantle density equal to 3.32 g/cm^3 and a water density of 1.05 g/cm^3, dH_W/dH_C can be computed for different crustal densities. For an average continental crustal density of $\rho_{cont} = 2.75$ g/cm^3, $dH_W/dH_C \approx -0.25$, and for an average oceanic crustal density of $\rho_{oc} = 2.9$ g/cm^3, $dH_W/dH_C \approx -0.19$. Thus, the estimated value of $dH_W/dH_C = -0.22$ is understood to be an average of the values expected if the Sea of Japan were composed homogeneously of either oceanic or continental crust. In fact, much of the scatter around the linear fit seen in Figure 18b is due to crustal heterogeneity across the sea. However, local isostasy may not be dominated by the crystalline crust alone, but may also be affected strongly by sediments and thermal buoyancy from the mantle, both of which have been ignored in the analysis here.

[56] Many different lines could, in fact, fit the data in Figure 18b nearly as well as the linear fit discussed above, which is presented with the solid red line. For example, if we assume that water depth, H_W, is the independent variable and solid crustal thickness, H_C, is the dependent variable, the least squares linear fit, shown with the dashed red line in Figure 18b, would be $H_W = -0.41\ H_C + 9.07$. Thus, a more careful analysis that considers lateral crustal heterogeneity, thermal buoyancy from the mantle, the effects of sediments, and uncertainties in the crustal thickness estimates is needed, but is beyond the scope of this paper. The results presented here demonstrate the reliability of the crustal thickness estimates across the Sea of Japan and also provide evidence that further analysis of the relation between seafloor depth and crustal thickness is warranted.

6.3. Lithospheric and Asthenospheric Structure Beneath the Sea of Japan

[57] Our 3-D model images what we refer to as a "Y-shaped" anomaly on vertical profiles with low-velocity arms reaching upward beneath the eastern and western borders of the Sea of Japan extending well into continental East Asia on the west side (e.g., Figure 17, profile A-A′), with an overlying ~60 km thick lithosphere beneath the Sea of Japan. The location of the lowest wave speeds at 80 km depth can be seen in Figure 19. In recent years, several other tomographic studies have been performed that are complementary to the ambient noise tomography presented here, which have imaged the mantle beneath the Sea of Japan. These studies possess greater depth penetration although lower resolution than our study and provide validation and assist with interpreting our results.

[58] Based on Rayleigh and Love wave phase velocities obtained from teleseismic earthquakes using the two-station

method, *Yoshizawa et al.* [2010] present a 3-D model of shear wave speeds from 40 to 200 km depth. Although their resolution is best beneath Japan and fades by the central Sea of Japan, their results in regions of good data coverage are similar to ours in several respects. First, they report an average lithospheric thickness beneath the Yamato Rise and the Japan Basin of 60 ± 10 km, which is similar to what we observe (e.g., Figure 17, profiles A-A′ and C′C′). Second, they also observe low-velocity anomalies at 75 km depth bordering Honshu beneath the eastern Sea of Japan and the East China Sea, west of the Ryukyu Islands. Thus, they also image the eastern arm of the Y-shaped anomaly that we report here and, like our model, observe it to migrate westward with depth. Their data coverage does not extend into East Asia. However, the teleseismic body wave study of *Zhao et al.* [2007] presented a large-scale image of the upper mantle beneath east Asia, which shows the stagnation of the subducted Pacific Plate beneath the Sea of Japan and clear low-velocity anomalies in the back-arc region. This study concentrates interpretation on the release of volatiles from the slab at several depths to produce the low-velocity anomalies observed in the back-arc region.

[59] Thus, *Yoshizawa et al.* [2010] serve to validate our model and *Zhao et al.* [2007] provide a means to interpret the Y-shaped anomaly based on what they call the "Big Mantle Wedge" model of the Japanese back arc and the devolatilization of the subducted slab. In their interpretation, the western arm of the Y-shaped anomaly beneath the western Sea of Japan and the East Asian Fold Belt would be caused by dehydration reactions of the stagnant slab in the mantle boundary layer (410–660 km). These warm hydrated upwellings are the cause of volcanism in East Asia (e.g., Changbai volcano) and may have precipitated the crustal rifting that led to the opening of the Sea of Japan. Presumably, the stagnant slab would generate hydrated plumes across the entire Sea of Japan, but the stretched and thinned continental lithosphere remains intact beneath the central Sea of Japan, as Figure 17 profiles A-A′ and C-C′ demonstrate, impeding upward migration of the hydrated plumes. These plumes would then become part of a westward directed convecting system that would amplify mantle hydration in the western Sea of Japan, near the rift margin. The eastern arm of the Y-shaped anomaly would be caused by slab dehydration at shallower depths, possibly caused by antigorite-related reactions. Thus, the Y-shaped anomaly reflects the details of shallow and deep slab dehydration and convective circulation in the mantle wedge above a stagnant slab.

6.4. Lithospheric Rejuvenation of the North China Craton

[60] The Chinese part of the Sino-Korean Craton, called the North China Craton (NCC), is composed of two Archean blocks, the eastern and the western NCC, which are separated by the central NCC. The central NCC is a Paleoproterozoic orogen called the Trans-North China Orogen. The three parts of the NCC are separated by dashed red lines in Figure 2. The NCC is believed to have cratonized by about 1.85 Ga, but the eastern NCC has undergone significant tectonothermal rejuvenation from the Ordovician to Cenozoic [*Menzies et al.*, 1993, 2007; *Griffin et al.*, 1998; *Gao et al.*, 2002, 2004; *Zhao et al.*, 2005, 2008]. These conclusions have been based on basalt-borne xenoliths and geophysical evidence for thin lithosphere (<100 km) with high heat flow in this region from the early Cenozoic to the present [e.g., *Menzies et al.*, 1993; *Griffin et al.*, 1998; *Fan et al.*, 2000; *Xu*, 2001; *Wu et al.*, 2005; *Chen et al.*, 2006, 2008, 2009]. Most studies agree that the central and western parts of the NCC have evolved differently than the eastern NCC during Phanerozoic time [e.g., *Xu et al.*, 2004; *Xu*, 2007], although some recent seismic studies point to localized lithospheric thinning in the central and even western NCC [e.g., *Huang et al.*, 2009; *Chen et al.*, 2009] and the generally high lateral heterogeneity of the lithosphere underlying the NCC. The mechanism of Phanerozoic lithospheric rejuvenation and its variability across the NCC remain intensely debated (see, e.g., *Chen* [2010] for a recent summary). Understanding of the Phanerozoic lithospheric tectonics would be improved with clearer images of the current structure of the crust, mantle lithosphere, and asthenosphere across the NCC.

[61] To this debate our 3-D model presents new relatively high-resolution images of the crust and uppermost mantle beneath most of the NCC. Crustal velocities beneath the eastern NCC are not particularly distinct from surrounding regions (e.g., Figure 14a), although the crust may be slightly thinner, on average (Figure 15a). More significantly, the eastern NCC hosts a "horseshoe" shaped anomaly in map view in the uppermost mantle, which is identified at 80 km depth in Figure 14d and, perhaps more clearly, by the blue contour in Figure 19. The velocities are lowest in the northern part of the North China Platform near the intersection of the North-South Gravity Lineament (NSGL) with the boundary between the central and eastern NCC. The low velocities continue southward, flanking the eastern NCC along the NSGL in the west and the TLF in the east. Low velocities also extend into small parts of the central NCC and the western NCC near the Datong Volcanoes. The south central part of the NCC is not particularly slow in the uppermost mantle as Figure 17 profile E-E′ illustrates, which reveals the considerable variability of lithospheric structure even within the eastern NCC.

[62] Within the "horseshoe" shaped anomaly bounding three sides of the eastern NCC (Figure 19), the lithosphere can be seen to be about 60 km thick on vertical profiles B-B′ and C-C′ of Figure 17. The flanks of the eastern NCC are underlain by asthenospheric low-velocity anomalies below 70 km depth as can be seen on profiles B-B′, C-C′, and E-E′. Profile B-B′ illustrates that the lithosphere is not simply thin; the velocities are lower than beneath the Songliao Basin to the north and the Ordos Block to the west. Thus, we hypothesize that the low-velocity anomalies that bound three sides of the eastern NCC identify a region of more intense tectonothermal activity than in south central part of the eastern NCC. Indeed, lithospheric rejuvenation may have reached nearly to the base of the crust in the most intensely altered zones.

7. Conclusions

[63] This paper presents a high-resolution 3-D shear velocity model of the crust and uppermost mantle with associated uncertainties across the North China Craton, northeastern China, the Korean Peninsula, and the Sea of Japan constructed from the dispersion characteristics of Rayleigh waves obtained from ambient noise cross correlations. Broadband stations from Chinese Provincial Networks,

the Japanese F-Net, and the IRIS GSN have produced 2 year continuous time series from 2007 into 2009 that form the basis for these results. Phase and group velocity maps from 8 s to 45 s period are first constructed, which constrain earth structures in the crust and uppermost mantle to a depth of about 100 km. The dispersion maps are geologically coherent, displaying the signatures of sedimentary basins, mountain roots, ocean-continent variations, and anomalies due to rifting and volcanism. The maps at different periods and between phase and group velocities are consistent with one another, and vertically relatively smooth Vsv models fit the observations.

[64] To generate the dispersion maps presented here, the effects of the persistent localized Kyushu microseism had to be eliminated in the dispersion measurements. We present a method based on locating the microseism (thereby confirming the location of *Zeng and Ni* [2010]), predicting the arrival of the disturbing signal on the ambient noise cross correlations, and obtaining the dispersion measurements by using the Green's functions at the opposite cross-correlation lag times for the station pairs in which the apparent speed of the Kyushu signal is less than 4.5 km/s.

[65] Ambient noise tomography places unique constraints on the structure of the crust and uppermost mantle, providing information complementary to body wave travel times, receiver functions, longer-period teleseismic surface waves, gravity, and other types of data. The motivation for the 3-D model is to produce new constraints on the volcanism, crustal extension, cratonic rejuvenation, and lithospheric thinning that are hypothesized for the region of study. The model presented here provides new information about these processes, particularly about the geometry (the geographic distribution and depth extent) of the observed features in the top 100 km. A detailed interpretation of the model is inconsistent with the scope of this paper, but we focus discussion on four principal model features: crustal thickness variations, particularly those associated with the North-South Gravity Lineament (NSGL) and beneath the Sea of Japan, the prominent but thin lithosphere underlying the Songliao-Bohai Graben, the "Y-shaped" mantle low-velocity anomaly (on vertical profiles) bordering the Sea of Japan, and a "horseshoe" shaped asthenospheric anomaly (in map view) bounding three sides of the eastern North China Craton.

[66] 1. The North-South Gravity Lineament is observed to follow approximately the 40 km crustal thickness contour. Beneath the Sea of Japan, crustal thickness is anticorrelated with water depth, and the relationship is consistent with expectations based on crustal isostasy for a laterally compositionally variable crust.

[67] 2. The Songliao-Bohai Graben is underlain by a high-velocity lower crust and a fast mantle lithosphere that extends to about 70 km depth. The lithosphere is not attenuated; that is seismic velocities are high, but it is thinner than expected for a region in which parts are traceable back to the Archean.

[68] 3. Low-velocity anomalies reach upward beneath the eastern and western borders of the Sea of Japan, extending well into continental East Asia on the west side. The arms of this Y-shaped anomaly are separated by the intervening overlying lithosphere, which is ~60 km thick and may represent stretched continental lithosphere. We argue that the Y-shaped structure in the east reflects relatively shallow slab dehydration and in the west deeper dehydration and convective circulation in the mantle wedge overlying the stagnant slab.

[69] 4. Very thin, attenuated lithosphere bounds three sides of the eastern North China Craton (NCC), but somewhat thicker faster lithosphere underlies the central and southern parts of the eastern NCC. These low-velocity anomalies identify a region of intense tectonothermal modification where lithospheric rejuvenation may have reached nearly to the base of the crust.

[70] In the future, assimilating similar results from a companion paper for southern China (Zhou et al., submitted manuscript, 2011) will allow the 3-D model to extend across all of eastern China. The geometry of the observing array makes the application of differential travel time methods for earthquakes difficult, such as eikonal tomography [*Lin et al.*, 2009], Helmholtz tomography [*Lin and Ritzwoller*, 2011], or two-plane wave tomography [e.g., *Yang et al.*, 2008b]. However, the success of such methods would allow dispersion maps to be extended to longer periods and, therefore, for the model to reach greater depths in the mantle. In addition to the production of a 3-D Vs model of the crust and uppermost mantle, other research envisioned includes the estimation of azimuthal anisotropy, which would place complementary constraints on the physical processes that motive this study. In addition, future understanding of the dispersion characteristics of Love waves would allow estimation of radial anisotropy, which reflects deformation undergone by the crust and uppermost mantle.

[71] **Acknowledgments.** The authors wish to thank An Yin and an anonymous reviewer for constructive criticism of an early draft and the AE for particularly insightful comments on a late draft of this paper. We are grateful to Anatoli Levshin, Fan-Chi Lin, and Shijie Zhong for valuable conversations. This work was performed while the first author visited the University of Colorado at Boulder over a period of one year. The work was supported by NSFC grant 40974034, CAS grant kzcx2-yw-142 and Y009021002, NSFC 41174086, CEA grant 201008007, US NSF-EAR award 0944022, and US NSF-OISE sub-award 0730154. This is contribution 20 from the ARC Centre of Excellence for Core to Crust Fluid Systems (http://www.ccfs.mq.edu.au) and 791 in the GEMOC Key Centre (http://www.gemoc.mq.edu.au). Most of the waveform data for this study were provided by the Data Management Centre of the China National Seismic Network at the Institute of Geophysics, China Earthquake Administration and F-Net in Japan. In addition, the facilities of the IRIS Data Management System were used to access data required in this study. The IRIS DMS is funded through the U.S. National Science Foundation under cooperative agreement EAR-0552316.

References

Bai, L., H. Kawakatsu, and Y. Morita (2010), Two anisotropic layers in central orogenic belt of the North China Craton, *Tectonophysics*, *494*, 138–148, doi:10.1016/j.tecto.2010.09.002.

Barmin, M. P., M. H. Ritzwoller, and A. L. Levshin (2001), A fast and reliable method for surface wave tomography, *Pure Appl. Geophys.*, *158*, 1351–1375, doi:10.1007/PL00001225.

Bassin, C., G. Laske, and G. Masters (2000), The current limits of resolution for surface wave tomography in North America, *Eos Trans. AGU*, *81*, F897.

Bensen, G. D., M. H. Ritzwoller, M. P. Barmin, A. L. Levshin, F. Lin, M. P. Moschetti, N. M. Shapiro, and Y. Yang (2007), Processing seismic ambient noise data to obtain reliable broad-band surface wave dispersion measurements, *Geophys. J. Int.*, *169*, 1239–1260, doi:10.1111/j.1365-246X.2007.03374.x.

Bensen, G. D., M. H. Ritzwoller, and N. M. Shapiro (2008), Broad-band ambient noise surface wave tomography across the United States, *J. Geophys. Res.*, *113*, B05306, doi:10.1029/2007JB005248.

Bensen, G. D., M. H. Ritzwoller, and Y. Yang (2009), A 3-D shear velocity model of the crust and uppermost mantle beneath the United States from ambient seismic noise, *Geophys. J. Int.*, *177*, 1177–1196, doi:10.1111/j.1365-246X.2009.04125.x.

Bourova, E., K. Yoshizawa, and K. Yomogida (2010), Upper mantle structure of marginal seas and subduction zones in northeastern Eurasia from Rayleigh wave tomography, *Phys. Earth Planet. Inter.*, *183*, 20–32, doi:10.1016/j.pepi.2010.06.007.

Chen, L. (2010), Concordant structural variations from the surface to the base of the upper mantle in the North China Craton and its tectonic implications, *Lithos*, *120*, 96–115, doi:10.1016/j.lithos.2009.12.007.

Chen, L., T. Zheng, and W. Xu (2006), A thinned lithospheric image of the Tanlu Fault Zone, eastern China: Constructed from wave equation based receiver function migration, *J. Geophys. Res.*, *111*, B09312, doi:10.1029/2005JB003974.

Chen, L., T. Wang, L. Zhao, and T. Zheng (2008), Distinct lateral variation of lithospheric thickness in the northeastern North China Craton, *Earth Planet. Sci. Lett.*, *267*, 56–68, doi:10.1016/j.epsl.2007.11.024.

Chen, L., C. Cheng, and Z. Wei (2009), Seismic evidence for significant lateral variations in lithospheric thickness beneath the central and western North China Craton, *Earth Planet. Sci. Lett.*, *286*, 171–183, doi:10.1016/j.epsl.2009.06.022.

Cho, K. H., R. B. Herrmann, C. J. Ammon, and K. Lee (2007), Imaging the upper crust of the Korean Peninsula by surface-wave tomography, *Bull. Seismol. Soc. Am.*, *97*(1B), 198–207, doi:10.1785/0120060096.

Christensen, N. I., and W. D. Mooney (1995), Seismic velocity structure and composition of the continental crust: A global view, *J. Geophys. Res.*, *100*, 9761–9788, doi:10.1029/95JB00259.

Deng, J., S. Su, Y. Niu, C. Liu, G. Zhao, X. Zhao, S. Zhou, and Z. Wu (2007), A possible model for the lithospheric thinning of the North China Craton: Evidence from the Yanshanian (Jura-Cretaceous) magmatism and tectonism, *Lithos*, *96*, 22–35, doi:10.1016/j.lithos.2006.09.009.

Dziewonski, A. M., and D. L. Anderson (1981), Preliminary reference Earth model, *Phys. Earth Planet. Inter.*, *25*, 297–356, doi:10.1016/0031-9201(81)90046-7.

Ekstrom, G., and A. M. Dziewonski (1997), Three-dimensional velocity structure of the Earth's upper mantle, in *Upper Mantle Heterogeneities From Active and Passive Seismology*, edited by K. Fuchs, pp. 187–198, Kluwer Acad., Norwell, Mass.

Fan, W., H. Zhang, J. Baker, K. Jarvis, P. R. D. Mason, and M. Menzies (2000), On and off the North China Craton: Where is the Archaean keel?, *J. Petrol.*, *41*(7), 933–950, doi:10.1093/petrology/41.7.933.

Fang, L., J. Wu, Z. Ding, and G. Panza (2010), High resolution Rayleigh wave group velocity tomography in North-China from ambient seismic noise, *Geophys. J. Int.*, *181*, 1171–1182.

Gao, S., R. Rudnick, R. Carlson, W. McDonough, and Y. Liu (2002), Re-Os evidence for replacement of ancient mantle lithosphere beneath the North China Craton, *Earth Planet. Sci. Lett.*, *198*, 307–322, doi:10.1016/S0012-821X(02)00489-2.

Gao, S., R. L. Rudnick, H.-L. Yuan, X.-M. Liu, Y.-S. Liu, W.-L. Xu, W.-L. Ling, J. Ayers, X. -C. Wang, and Q. -H. Wang (2004), Recycling lower continental crust in the North China Craton, *Nature*, *432*, 892–897, doi:10.1038/nature03162.

Griffin, W. L., A. Zhang, S. Y. O'Reilly, and C. Ryan (1998), Phanerozoic evolution of the lithosphere beneath the Sino-Korean Craton, in *Mantle Dynamics and Plate Interactions in East Asia*, *Geodyn. Ser.*, vol. 27, edited by M. Flower et al., pp. 107–126, AGU, Washington, D. C., doi:10.1029/GD027p0107.

Guo, Z., X. Gao, H. Yao, J. Li, and W. Wang (2009), Midcrustal low-velocity layer beneath the central Himalaya and southern Tibet revealed by ambient noise array tomography, *Geochem. Geophys. Geosyst.*, *10*, Q05007, doi:10.1029/2009GC002458.

He, Z., T. Ye, and Z. Ding (2009), Surface wave tomography for the phase velocity in the northeastern part of North China, *Chin. J. Geophys.*, *52*(5), 1233–1242.

Huang, H., H. Yao, and R. D. van der Hilst (2010), Radial anisotropy in the crust of SE Tibet and SW China from ambient noise interferometry, *Geophys. Res. Lett.*, *37*, L21310, doi:10.1029/2010GL044981.

Huang, J., and D. Zhao (2006), High-resolution mantle tomography of China and surrounding regions, *J. Geophys. Res.*, *111*, B09305, doi:10.1029/2005JB004066.

Huang, Z., W. Su, Y. Peng, Y. Zheng, and H. Li (2003), Rayleigh wave tomography of China and adjacent regions, *J. Geophys. Res.*, *108*(B2), 2073, doi:10.1029/2001JB001696.

Huang, Z., Y. Peng, Y. Luo, Y. Zheng, and W. Su (2004), Azimuthal anisotropy of Rayleigh waves in East Asia, *Geophys. Res. Lett.*, *31*, L15617, doi:10.1029/2004GL020399.

Huang, Z., H. Li, Y. Zheng, and Y. Peng (2009), The lithosphere of North China Craton from surface wave tomography, *Earth Planet. Sci. Lett.*, *288*, 164–173, doi:10.1016/j.epsl.2009.09.019.

Jolivet, L. K., K. Tamaki, and M. Fournier (1994), Japan Sea, opening history and mechanism: A synthesis, *J. Geophys. Res.*, *99*, 22,237–22,259, doi:10.1029/93JB03463.

Kanamori, H., and D. L. Anderson (1977), Importance of physical dispersion in surface wave and free oscillation problems: Review, *Rev. Geophys.*, *15*(1), 105–112, doi:10.1029/RG015i001p00105.

Kang, T. S., and J. S. Shin (2006), Surface-wave tomography from ambient seismic noise of accelerograph networks in southern Korea, *Geophys. Res. Lett.*, *33*, L17303, doi:10.1029/2006GL027044.

Kawakatsu, H., M. Yamamoto, S. Kaneshima, and T. Ohkura (2011), Comment on "A persistent localized microseismic source near the Kyushu Island, Japan" by Xiangfang Zeng and Sidao Ni, *Geophys. Res. Lett.*, *38*, L17307, doi:10.1029/2011GL048584.

Kurashimo, E., M. Shinohara, K. Suyehiro, J. Kasahara, and N. Hirata (1996), Seismic evidence for stretched continental crust in the Japan Sea, *Geophys. Res. Lett.*, *23*, 3067–3070, doi:10.1029/96GL02765.

Lebedev, S., and G. Nolet (2003), Upper mantle beneath Southeast Asia from *S* velocity tomography, *J. Geophys. Res.*, *108*(B1), 2048, doi:10.1029/2000JB000073.

Levshin, A., M. H. Ritzwoller, and J. Resovsky (1999), Source effects on surface wave group travel times and group velocity maps, *Phys. Earth Planet. Inter.*, *115*, 293–312, doi:10.1016/S0031-9201(99)00113-2.

Levshin, A., M. Barmin, M. H. Ritzwoller, and J. Trampert (2005), Minor-arc and major-arc global surface wave diffraction tomography, *Phys. Earth Planet. Inter.*, *149*, 205–223, doi:10.1016/j.pepi.2004.10.006.

Li, C., and R. D. van der Hilst (2010), Structure of the upper mantle and transition zone beneath Southeast Asia from traveltime tomography, *J. Geophys. Res.*, *115*, B07308, doi:10.1029/2009JB006882.

Li, H. Y., W. Su, C. Y. Wang, and Z. X. Huang (2009), Ambient noise Rayleigh wave tomography in western Sichuan and eastern Tibet, *Earth Planet. Sci. Lett.*, *282*, 201–211, doi:10.1016/j.epsl.2009.03.021.

Li, J., and F. Niu (2010), Seismic anisotropy and mantle flow beneath northeast China inferred from regional seismic networks, *J. Geophys. Res.*, *115*, B12327, doi:10.1029/2010JB007470.

Li, Z., T. Hao, and Y. Xu (2011), Uppermost mantle structure of the North China Craton: Constraints from interstation Pn travel time difference tomography, *Chin. Sci. Bull.*, *56*, 1691–1698, doi:10.1007/s11434-011-4487-y.

Lin, F. C., and M. H. Ritzwoller (2011), Helmholtz surface wave tomography for isotropic and azimuthally anisotropic structure, *Geophys. J. Int.*, *186*, 1104–1120, doi:10.1111/j.1365-246X.2011.05070.x.

Lin, F. C., M. H. Ritzwoller, J. Townend, S. Bannister, and M. K. Savage (2007), Ambient noise Rayleigh wave tomography of New Zealand, *Geophys. J. Int.*, *170*, 649–666, doi:10.1111/j.1365-246X.2007.03414.x.

Lin, F. C., M. P. Moschetti, and M. H. Ritzwoller (2008), Surface wave tomography of the western United States from ambient seismic noise: Rayleigh and Love wave phase velocity maps, *Geophys. J. Int.*, *173*, 281–298, doi:10.1111/j.1365-246X.2008.03720.x.

Lin, F. C., M. H. Ritzwoller, and R. Snieder (2009), Eikonal tomography: Surface wave tomography by phase front tracking across a regional broad-band seismic array, *Geophys. J. Int.*, *177*, 1091–1110.

Lin, F. C., M. H. Ritzwoller, Y. Yang, M. Moschetti, and M. Fouch (2011), Complex and variable crustal and uppermost mantle seismic anisotropy in the western United States, *Nat. Geosci.*, *4*(1), 55–61, doi:10.1038/ngeo1036.

Liu, J., J. Han, and W. Fyfe (2001), Cenozoic episodic volcanism and continental rifting in northeast China and possible link to Japan Sea development as revealed from K-Ar geochronology, *Tectonophysics*, *339*, 385–401, doi:10.1016/S0040-1951(01)00132-9.

Menzies, M. A., W. Fan, and M. Zhang (1993), Paleozoic and Cenozoic lithoprobes and the loss of >120 km of Archaean lithosphere, Sino-Korean craton, China, *Geol. Soc. Spec. Publ.*, *76*, 71–81, doi:10.1144/GSL.SP.1993.076.01.04.

Menzies, M., Y. Xu, H. Zhang, and W. Fan (2007), An integration of geology, geophysics, and geochemistry: A key to understanding the North China Craton, *Lithos*, *96*, 1–21, doi:10.1016/j.lithos.2006.09.008.

Moschetti, M. P., M. H. Ritzwoller, and N. M. Shapiro (2007), Surface wave tomography of the western United States from ambient seismic noise: Rayleigh wave group velocity maps, *Geochem. Geophys. Geosyst.*, *8*, Q08010, doi:10.1029/2007GC001655.

Moschetti, M. P., M. H. Ritzwoller, F. Lin, and Y. Yang (2010a), Seismic evidence for widespread western-US deep-crustal deformation caused by extension, *Nature*, *464*, 885–889, doi:10.1038/nature08951.

Moschetti, M. P., M. H. Ritzwoller, F. C. Lin, and Y. Yang (2010b), Crustal shear wave velocity structure of the western United States

inferred from ambient noise and earthquake data, *J. Geophys. Res.*, *115*, B10306, doi:10.1029/2010JB007448.
Mosegaard, K., and A. Tarantola (1995), Monte Carlo sampling of solutions to inverse problems, *J. Geophys. Res.*, *100*, 12,431–12,447, doi:10.1029/94JB03097.
Nishida, K., H. Kawakatsu, and K. Obara (2008), Three-dimensional crustal *S* wave velocity structure in Japan using microseismic data recorded by Hi-net tiltmeters, *J. Geophys. Res.*, *113*, B10302, doi:10.1029/2007JB005395.
Okada, Y., K. Kasahara, S. Hori, K. Obara, S. Sekiguchi, H. Fujiwara, and A. Yamamoto (2004), Recent progress of seismic observation networks in Japan-Hi-net, F-net, K-NET and KiK-net, *Earth Planets Space*, *56*, 15–28.
Pan, J., Q. Wu, Y. Li, F. Zhang, and G. Zhang (2011), Rayleigh wave tomography of the phase velocity in North China, *Chin. J. Geophys.*, *54*(1), 67–76.
Priestley, K., E. Debayle, D. McKenzie, and S. Pilidou (2006), Upper mantle structure of eastern Asia from multimode surface waveform tomography, *J. Geophys. Res.*, *111*, B10304, doi:10.1029/2005JB004082.
Ren, J., K. Tamaki, S. Li, and J. Zhang (2002), Late Mesozoic and Cenozoic rifting and its dynamic setting in eastern China and adjacent seas, *Tectonophysics*, *344*, 175–205, doi:10.1016/S0040-1951(01)00271-2.
Ritzwoller, M. H., and A. Levshin (1998), Eurasian surface wave tomography: Group velocities, *J. Geophys. Res.*, *103*, 4839–4878, doi:10.1029/97JB02622.
Ritzwoller, M. H., A. Levshin, L. Ratnikova, and A. Egorkin (1998), Intermediate period group velocity maps across central Asia, western China, and parts of the Middle East, *Geophys. J. Int.*, *134*, 315–328.
Rogers, J. J. W., and M. Santosh (2006), The Sino-Korean Craton and supercontinent history: Problems and perspectives, *Gondwana Res.*, *9*, 21–23, doi:10.1016/j.gr.2005.04.001.
Sabra, K. G., P. Gerstoft, P. Roux, W. A. Kuperman, and M. C. Fehler (2005), Surface wave tomography from microseisms in Southern California, *Geophys. Res. Lett.*, *32*, L14311, doi:10.1029/2005GL023155.
Santosh, M., D. Zhao, and T. Kusky (2010), Mantle dynamics of the Paleoproterozoic North China Craton: A perspective based on seismic tomography, *J. Geodyn.*, *49*, 39–53, doi:10.1016/j.jog.2009.09.043.
Sato, T., M. Shinohara, B. Y. Karp, R. G. Kulinich, and N. Isezaki (2004), *P* wave velocity structure in the northern part of the central Japan Basin, Japan Sea with ocean bottom seismometers and airguns, *Earth Planets Space*, *56*, 501–510.
Sengor, A. M. C., and B. A. Natal'in (1996), Paleotectonics of Asia: Fragments of a synthesis, in *The Tectonic Evolution of Asia*, edited by A. Yin and T. M. Harrison, pp. 486–640, Cambridge Univ. Press, New York.
Shapiro, N. M., and M. H. Ritzwoller (2002), Monte-Carlo inversion for a global shear-velocity model of the crust and upper mantle, *Geophys. J. Int.*, *151*, 88–105, doi:10.1046/j.1365-246X.2002.01742.x.
Shapiro, N. M., M. H. Ritzwoller, P. Molnar, and V. Levin (2004), Thinning and flow of Tibetan crust constrained by seismic anisotropy, *Science*, *305*, 233–236, doi:10.1126/science.1098276.
Shapiro, N. M., M. Campillo, L. Stehly, and M. H. Ritzwoller (2005), High-resolution surface wave tomography from ambient seismic noise, *Science*, *307*, 1615–1618, doi:10.1126/science.1108339.
Shapiro, N. M., M. H. Ritzwoller, and G. D. Bensen (2006), Source location of the 26 sec microseism from cross correlations of ambient seismic noise, *Geophys. Res. Lett.*, *33*, L18310, doi:10.1029/2006GL027010.
Sun, X., X. Song, S. Zheng, Y. Yang, and M. H. Ritzwoller (2010), Three dimensional shear wave velocity structure of the crust and upper mantle beneath China from ambient noise surface wave tomography, *Earthquake Sci.*, *23*, 449–463, doi:10.1007/s11589-010-0744-4.
Sun, Y., and M. N. Toksöz (2006), Crustal structure of China and surrounding regions from *P* wave traveltime tomography, *J. Geophys. Res.*, *111*, B03310, doi:10.1029/2005JB003962.
Taira, A. (2001), Tectonic evolution of the Japanese island arc system, *Annu. Rev. Earth Planet. Sci.*, *29*, 109–134, doi:10.1146/annurev.earth.29.1.109.
Tamaki, K., K. Suychiro, J. Allan, J. C. Ingle Jr., and K. A. Pisciotto (1992), Tectonic synthesis and implications of Japan Sea ODP Drilling, *Proc. Ocean Drill. Program Sci. Results*, *127/128*(2), 1333–1348.
Tang, Q., and L. Chen (2008), Structure of the crust and uppermost mantle of the Yanshan Belt and adjacent regions at the northeastern boundary of the North China Craton from Rayleigh wave dispersion analysis, *Tectonophysics*, *455*, 43–52, doi:10.1016/j.tecto.2008.04.021.
Tatsumi, Y., Y. Otofuji, T. Matsuda, and S. Nohda (1989), Opening of the Sea of Japan back-arc basin by asthenospheric injection, *Tectonophysics*, *166*, 317–329, doi:10.1016/0040-1951(89)90283-7.
Tian, A. Y., P. Han, and K. D. Xu (1992), The Mesozoic-Cenozoic East China rift system, *Tectonophysics*, *208*, 341–363, doi:10.1016/0040-1951(92)90354-9.
Tian, Y., D. Zhao, R. Sun, and J. Teng (2009), Seismic imaging of the crust and upper mantle beneath the North China Craton, *Phys. Earth Planet. Inter.*, *172*, 169–182, doi:10.1016/j.pepi.2008.09.002.
Villaseñor, A., M. H. Ritzwoller, A. L. Levshin, M. P. Barmin, E. R. Engdahl, W. Spakman, and J. Trampert (2001), Shear velocity structure of central Eurasia from inversion of surface wave velocities, *Phys. Earth Planet. Inter.*, *123*, 169–184, doi:10.1016/S0031-9201(00)00208-9.
Villaseñor, A., Y. Yang, M. H. Ritzwoller, and J. Gallart (2007), Ambient noise surface wave tomography of the Iberian Peninsula: Implication's for shallow seismic structure, *Geophys. Res. Lett.*, *34*, L11304, doi:10.1029/2007GL030164.
Wu, F., J. Lin, A. Simon, X. Zhang, and J. Yang (2005), Nature and significance of the Early Cretaceous giant igneous event in eastern China, *Earth Planet. Sci. Lett.*, *233*, 103–119, doi:10.1016/j.epsl.2005.02.019.
Xu, P., and D. Zhao (2009), Upper-mantle velocity structure beneath the North China Craton: Implications for lithospheric thinning, *Geophys. J. Int.*, *177*, 1279–1283, doi:10.1111/j.1365-246X.2009.04120.x.
Xu, Y. G. (2001), Thermo-tectonic destruction of the Archaean lithospheric keel beneath the Sino-Korean craton in China: Evidence, timing and mechanism, *Phys. Chem. Earth, Part A*, *26*, 747–757, doi:10.1016/S1464-1895(01)00124-7.
Xu, Y. G. (2007), Diachronous lithospheric thinning of the North China Craton and formation of the Daxin'anling-Taihangshan gravity lineament, *Lithos*, *96*, 281–298, doi:10.1016/j.lithos.2006.09.013.
Xu, Y. G., S. L. Chung, J. L. Ma, and L. B. Shi (2004), Contrasting Cenozoic lithospheric evolution and architecture in the eastern and western Sino-Korean craton: Constraints from geochemistry of basalts and mantle xenoliths, *J. Geol.*, *112*, 593–605, doi:10.1086/422668.
Yang, Y., and M. H. Ritzwoller (2008), Characteristics of ambient seismic noise as a source for surface wave tomography, *Geochem. Geophys. Geosyst.*, *9*, Q02008, doi:10.1029/2007GC001814.
Yang, Y., M. H. Ritzwoller, A. L. Levshin, and N. M. Shapiro (2007), Ambient noise Rayleigh wave tomography across Europe, *Geophys. J. Int.*, *168*, 259–274, doi:10.1111/j.1365-246X.2006.03203.x.
Yang, Y., A. Li, and M. Ritzwoller (2008a), Crustal and uppermost mantle structure in southern Africa revealed from ambient noise and teleseismic tomography, *Geophys. J. Int.*, *174*, 235–248, doi:10.1111/j.1365-246X.2008.03779.x.
Yang, Y., M. H. Ritzwoller, F. C. Lin, M. P. Moschetti, and N. M. Shapiro (2008b), Structure of the crust and uppermost mantle beneath the western United States revealed by ambient noise and earthquake tomography, *J. Geophys. Res.*, *113*, B12310, doi:10.1029/2008JB005833.
Yang, Y., et al. (2010), Rayleigh wave phase velocity maps of Tibet and the surrounding regions from ambient seismic noise tomography, *Geochem. Geophys. Geosyst.*, *11*, Q08010, doi:10.1029/2010GC003119.
Yanovskaya, T. B., and V. M. Kozhevnikov (2003), 3D *S*-wave velocity pattern in the upper mantle beneath the continent of Asia from Rayleigh wave data, *Phys. Earth Planet. Inter.*, *138*, 263–278, doi:10.1016/S0031-9201(03)00154-7.
Yao, H., R. D. van der Hilst, and M. V. de Hoop (2006), Surface-wave array tomography in SE Tibet from ambient seismic noise and two-station analysis—I. Phase velocity maps, *Geophys. J. Int.*, *166*, 732–744, doi:10.1111/j.1365-246X.2006.03028.x.
Yao, H., C. Beghein, and R. D. van der Hilst (2008), Surface wave array tomography in SE Tibet from ambient seismic noise and two-station analysis—II. Crustal and upper-mantle structure, *Geophys. J. Int.*, *173*, 205–219, doi:10.1111/j.1365-246X.2007.03696.x.
Yin, A. (2010), Cenozoic tectonic evolution of Asia: A preliminary synthesis, *Tectonophysics*, *488*, 293–325, doi:10.1016/j.tecto.2009.06.002.
Yin, A., and S. Nie (1993), An indentation model for the North and South China collision and the development of the Tan-Lu and Honam Fault systems, eastern Asia, *Tectonics*, *12*(4), 801–813, doi:10.1029/93TC00313.
Yin, A., and S. Nie (1996), A Phanerozoic palinspastic reconstruction of China and its neighboring regions, in *The Tectonic Evolution of Asia*, edited by A. Yin and T. M. Harrison, pp. 442–485, Cambridge Univ. Press, New York.
Yoshizawa, K., K. Miyake, and K. Yomogida (2010), 3D upper mantle structure beneath Japan and its surrounding region from inter-station measurements of surface waves, *Phys. Earth Planet. Inter.*, *183*, 4–19, doi:10.1016/j.pepi.2010.02.012.
Zeng, X., and S. Ni (2010), A persistent localized microseismic source near the Kyushu Island, Japan, *Geophys. Res. Lett.*, *37*, L24307, doi:10.1029/2010GL045774.
Zeng, X., and S. Ni (2011), Correction to "A persistent localized microseismic source near the Kyushu Island, Japan," *Geophys. Res. Lett.*, *38*, L16320, doi:10.1029/2011GL048822.

Zhang, P., Q. Deng, G. Zhang, J. Ma, W. Gan, W. Min, F. Mao, and Q. Wang (2003), Active tectonic blocks and strong earthquake in the continent of China, *Sci. China Ser. D*, *46*, suppl. 2, 13–24.

Zhao, D. (2009), Multiscale seismic tomography and mantle dynamics, *Gondwana Res.*, *15*, 297–323, doi:10.1016/j.gr.2008.07.003.

Zhao, D., S. Maruyama, and S. Omori (2007), Mantle dynamics of western Pacific and East Asia: Insight from seismic tomography and mineral physics, *Gondwana Res.*, *11*, 120–131, doi:10.1016/j.gr.2006.06.006.

Zhao, G., M. Sun, S. A. Wilde, and S. Li (2005), Late Archean to Paleoproterozoic evolution of the North China Craton: Key issues revisited, *Precambrian Res.*, *136*, 177–202, doi:10.1016/j.precamres.2004.10.002.

Zhao, L., T. Zheng, and G. Lu (2008), Insight into craton evolution: Constraints from shear wave splitting in the North China Craton, *Phys. Earth Planet. Inter.*, *168*, 153–162, doi:10.1016/j.pepi.2008.06.003.

Zheng, S., X. Sun, X. Song, Y. Yang, and M. H. Ritzwoller (2008), Surface wave tomography of China from ambient seismic noise correlation, *Geochem. Geophys. Geosyst.*, *9*, Q05020, doi:10.1029/2008GC001981.

Zheng, T., L. Chen, L. Zhao, W. Xu, and R. Zhu (2006), Crust-mantle structure difference across the gravity gradient zone in North China Craton: Seismic image of the thinned continental crust, *Phys. Earth Planet. Inter.*, *159*, 43–58, doi:10.1016/j.pepi.2006.05.004.

Zheng, X. F., Z. X. Yao, J. H. Liang, and J. Zheng (2010a), The role played and opportunities provided by IGP DMC of China National Seismic Network in Wenchuan earthquake disaster relief and researches, *Bull. Seismol. Soc. Am.*, *100*(5B), 2866–2872, doi:10.1785/0120090257.

Zheng, Y., Y. Yang, M. H. Ritzwoller, X. Zheng, X. Xiong, and Z. Li (2010b), Crustal structure of the northeastern Tibetan Plateau, the Ordos Block and the Sichuan Basin from ambient noise tomography, *Earthquake Sci.*, *23*, 465–476, doi:10.1007/s11589-010-0745-3.

Zhou, R. M., B. W. Stump, R. B. Herrmann, Z. X. Yang, and Y. T. Chen (2009), Teleseismic receiver function and surface-wave study of velocity structure beneath the Yanqing-Huailai Basin northwest of Beijing, *Bull. Seismol. Soc. Am.*, *99*(3), 1937–1952, doi:10.1785/0120080277.

M. H. Ritzwoller and W. Shen, Center for Imaging the Earth's Interior, Department of Physics, University of Colorado at Boulder, Boulder, CO 80309-0390, USA. (michael.ritzwoller@colorado.edu)

Z. Xie and Y. Zheng, State Key Laboratory of Geodesy and Earth's Dynamics, Institute of Geodesy and Geophysics, Chinese Academy of Sciences, Wuhan, Hubei 430077, China. (zhengyong@whigg.ac.cn)

Y. Yang, Australian Research Council Centre of Excellence for Core to Crust Fluid Systems/GEMOC, Department of Earth and Planetary Sciences, Macquarie University, North Ryde, NSW 2109, Australia. (yingjie.yang@mq.edu.au)

L. Zhou, China Earthquake Network Center, Beijing 100045, China. (lqzhou@seis.ac.cn)